

**The Pennsylvania State University**  
**The Graduate School**  
**College of Earth and Mineral Sciences**

**Reservoir Pressure and Sea Floor Venting: Predicting trap  
integrity in a Gulf of Mexico deepwater turbidite minibasin**

**A Thesis in**  
**Geosciences**  
**by**  
**Benjamin John Seldon**

**Copyright 2003 Benjamin John Seldon**

**Submitted in Partial Fulfillment  
of the Requirements  
for the Degree of**

**Master of Science**

**December 2003**

The thesis of Benjamin John Seldon was reviewed and approved\* by the following:

**Peter B. Flemings**  
**Associate Professor of Geosciences**  
**Thesis Advisor**

**Rudy L. Slingerland**  
**Professor of Geology**

**Christopher J. Marone**  
**Professor of Geosciences**

**Nicholas Harris**  
**Senior Scientist**

**Peter Deines**  
**Professor of Geochemistry**  
**Associate Head for Graduate Programs and Research**

\*Signatures are on file in the Graduate School

**I grant The Pennsylvania State University the non-exclusive right to use this work for the University's own purposes and to make single copies of the work available to the public on a not-for-profit basis if copies are not otherwise available.**

---

**Benjamin John Seldon**

## **Abstract**

Pore pressures at the crest of two sands in the Popeye/Genesis deepwater Gulf of Mexico minibasin (GC72/GC205) equal the least principal stress. We interpret that sand pore pressures, elevated by flow focusing, are dilating fractures in the cap rock, inducing fluid migration from the crest. These 'leak points' limit the reservoir pressure to the least principal stress at the crest and ultimately ensure the integrity of the cap rock trapping the hydrocarbons at the offset Genesis and Popeye fields. An active fault provides a migration pathway between the crests and the seafloor which is characterized by gas hydrate deposits and fluid venting from mud volcanoes. Direct pressure measurements are used to estimate the pore pressures and the least principal stresses are constrained by leak-off measurements. We infer that in geopressured basins with significant structural relief where the pore pressures at the structural crest of the reservoir body equal the least principal stress, fluids expulsion results. With evidence of these conditions, it is possible to predict the effective-stress state throughout the basin, which allows for the estimation of trap integrity at subsidiary structures and the design of safe and economic drilling programs.

# Contents

<b>List of Figures</b>	<b>v</b>
<b>List of Tables</b>	<b>vii</b>
<b>Acknowledgements</b>	<b>viii</b>
<b>Chapter 1: Preface</b>	<b>1</b>
<b>Chapter 2: Reservoir Pressure and Sea Floor Venting: Predicting trap integrity in a Gulf of Mexico deepwater turbidite minibasin</b>	
<b>2.1 Introduction</b>	<b>4</b>
<b>2.2 Structure and Geology of the Popeye-Genesis minibasin</b>	<b>5</b>
<b>2.2.1 Reservoir Characterization and depositional setting</b>	<b>8</b>
<b>2.3 Pressure, Stress and Trap Integrity</b>	<b>12</b>
<b>2.3.1 Principal Stresses</b>	<b>12</b>
<b>2.3.2 Reservoir Pressures</b>	<b>15</b>
<b>2.3.3 Definition of a Minibasin Leak-point</b>	<b>19</b>
<b>2.4 Seafloor Expulsion System</b>	<b>20</b>
<b>2.5 Discussion and Applications</b>	<b>24</b>
<b>2.6 Conclusions</b>	<b>29</b>
<b>2.8 Appendix A: Methodology for estimation of overburden stresses</b>	<b>31</b>
<b>2.9 References</b>	<b>33</b>

## List of Figures

1		Popeye-Genesis minibasin location	6
2	a	Structure map of minibasin reservoir sands	7
	b	Cartoon cross-section of the minibasin	7
3		Amplitude extraction of key minibasin reservoir	8
4	a	Depth structure of the F1-sand	10
	b	Depth structure of the G-sand	10
	c	Depth structure of the N1-sand	10
5		Correlated log cross-section of reservoir sands	11
6		Bounding stresses of the minibasin	13
7	a	Reservoir pressures of the F1-sand	16
	b	Reservoir pressures of the G-sand	16
	c	Reservoir pressures of the N-sands	16
8	a	Pressure-depth plot characterizing sand pressures	18
	b	Structural cartoon displaying sand overpressures	18
9	a	Amplitude characteristics of the seafloor horizon over seafloor expulsion features	21
	b	Shallow time cross-section of the expulsion feature (S)	21
	c	Deep time cross-section of the expulsion feature (S)	22
	d	Deep time cross-section of the mud volcano (N)	22
10	a	Geologic cartoon and parallel pressure-depth plot summarizing the leak-point control	25
11	a	Pressure-depth plot characterizing sand failure for	27



## List of Tables

<b>2.1</b>	<b>Estimated overpressures and overburdens</b>	<b>11</b>
<b>2.2</b>	<b>LOT data summary</b>	<b>14</b>
<b>2.3</b>	<b>RFT data and structural summary</b>	<b>17</b>
<b>2.4</b>	<b>Fluid Density Gradients</b>	<b>17</b>
<b>2.5</b>	<b>Nomenclature</b>	<b>32</b>

## Acknowledgements

I consider my time in the Penn State Geosciences department to have been a great personal and academic success largely through the enthusiasm of my colleagues, supervisors and the support of my family and friends.

I am forever indebted to my mother Antonia, my father Roger, my sister Beth and my Grandfather John-Henry for their love and support in difficult times and a selflessness that has afforded me this opportunity.

From the outset Beth, Christine (Jean Wiley) and Eric have been the most inspiring, enthusiastic and patient of officemates. I believe I have personally placed more stress on these three individuals than anyone else in my life; they have handled my bizarre foreign and personal customs with understanding and compassion.

I wish to thank my University Club brothers Alex, Gavin, Jaime, Jay and Mikey for keeping me sane over the last two years and providing me with more laughs than a guy deserves.

Heather, Rachel, Stef-bomb and Frank are sited for saving my posterior on numerous occasions and providing me with the resources needed to complete my research. If I there was an award for dedication in the face adversity it would go straight to Tom Canich. He has helped me in countless battles against software, hardware and my own

ineptitude and his bountiful caffeine supplies have kept motivated on numerous occasions.

Both Brandon Dugan and Jacek Lupa have been a continual source of inspiration and advice even after their departure from Penn State. They ensured I have been 'macked-out' with constructive criticism and comic relief. Brandon in particular displayed incredible patience and enthusiasm while familiarizing me with applications and concepts. I consider myself very fortunate to have had such a mentor and friend. So good!

Peter B. Flemings is unique. I have yet to meet a man with such drive and intelligence who is willing to support a student who makes his life anything but easy (e.g. rock hammers at airport security). His unflinching enthusiasm and dedication and have pushed me to areas of research which until now seemed untenable and have provided me with a professional position of choice.

# Chapter 1: Preface

This thesis is composed of three chapters. This chapter summarizes the contents and the contributing parties of the work presented in Chapters 2 and 3.

## **Chapter 2: Reservoir Pressure and Sea Floor Venting: Predicting trap integrity in a Gulf of Mexico deepwater turbidite minibasin**

The second chapter represents my individual research completed during my time with the Petroleum Geosystems Initiative (Team 2) and Geofluids II consortium in the Penn State Geosciences Department.

Datasets from both Popeye and Genesis fields, Green Canyon 72 and 205, Gulf of Mexico provide the foundation for a minibasin-scale fluid flow study which illustrate how fluid expulsion at a minibasin leak-point links hydrocarbon trap integrity and seafloor expulsion features. The leak-point, defined by the convergence of sand pore pressures and the least-principal stress, underlies a series of seafloor expulsion features. Fluid expulsion at this leak-point maintains the trap integrities of the minibasin hydrocarbon accumulations, produces an inverted overpressure profile through the minibasin sands and contributes fluids to the overlying seafloor expulsion features. An updated summary of the expulsion system is included drawing on 3-D seismic data, direct observations from submersible dives and recent geochemical studies comparing fluids vented at the seafloor and stored at the Genesis Field.

These observations are used to propose a simple predictive method for mapping and evaluating protected traps associated with fluid expulsion. The method assumes particular significance at a time when exploration companies are searching worldwide for analogies to Gulf of Mexico plays.

### **Chapter 3: Integration of Geologic Model and Reservoir Simulation, Popeye Field, Green Canyon 116**

The third chapter is an insert of a joint paper submitted and presented by the Petroleum Geosystems Initiative (Team 2), Penn State University to the Gulf Coast Association of Geological Societies Annual meeting 2003. The insert is in published galley format with written permission from the Pennsylvania State University Thesis Office.

Well log, engineering, and seismic data were integrated to develop a depositional model for the Popeye field. The depositional model provides constraints for the sand distribution interpretations used in reservoir simulations. Integration of seismic mapping of the complex structure of the field and simulation results elucidate several key geologic uncertainties which are explored through modification of a base-case model.

The base-case reservoir simulation results in a volume of bypassed reserves within the compartmentalized reservoirs. The location and amount of un-recovered reserves differs based on the modeled fault separation between these compartments, aquifer volume, and the transmissibility of an erosional bounding channel. Reasonable variations in these geologic model features significantly influence reservoir drainage behavior.

## **Chapter 2: Reservoir Pressure and Sea Floor Venting: Predicting trap integrity in a Gulf of Mexico deepwater turbidite minibasin**

### **Abstract**

Pore pressures at the crest of two sands in the Popeye/Genesis deepwater Gulf of Mexico minibasin (GC72/GC205) equal the least principal stress. We interpret that sand pore pressures, elevated by flow focusing, are dilating fractures in the cap rock, inducing fluid migration from the crest. These 'leak points' limit the reservoir pressure to the least principal stress at the crest and ultimately ensure the integrity of the cap rock trapping the hydrocarbons at the offset Genesis and Popeye fields. An active fault provides a migration pathway between the crests and the seafloor which is characterized by gas hydrate deposits and fluid venting from mud volcanoes. Direct pressure measurements are used to estimate the pore pressures and the least principal stresses are constrained by leak-off measurements.

We infer that in geopressured basins with significant structural relief where the pore pressures at the structural crest of the reservoir body equal the least principal stress, fluids expulsion results. With evidence of these conditions, it is possible to predict the effective-stress state throughout the basin, which allows for the estimation of trap integrity at subsidiary structures and the design of safe and economic drilling programs.

## 2.1. Introduction

Seafloor fluid expulsion is associated with petroleum exploration hazards, economic gas hydrate accumulations, and climate change (Dickens et al., 1997; Lerche and Bagirov, 1998; Milkov, 2000; Milkov and Sassen, 2001; Etiope and Klusman, 2002). The seafloor emission of hydrocarbons have been characterized worldwide (Roberts and Carney, 1997; Milkov, 2000; Somoza et al., 2003). In the study area (Green Canyon, Gulf of Mexico) seafloor emissions have been compared to their deeper petroleum system sources in an effort to understand their genesis and migration (Brooks et al., 1986; Boettcher and Abrams, 2000; Sassen et al., 2003). A commonly cited but rarely quantified source for these fluid flow systems is fluid expulsion from overpressured bodies.

Overpressured pore fluids develop in basins where the rate of sedimentation exceeds the ability of the fluids to freely escape, forcing the pore fluids to support some fraction of the overlying load (Harrison and Summa, 1991; Gaarenstroom et al., 1993; Swarbrick et al., 2000). When dipping, permeable sandstone bodies are encased in overpressured low permeability mudstone a characteristic pressure field develops: sandstone pore pressures follow the hydrostatic gradient while mudstone pressures exhibit a steeper (often lithostatic) gradient (Dugan and Flemings, 2000; Yardley and Swarbrick, 2000; Flemings et al., 2002). This contrast in gradients elevates the pore pressures at the sand crest relative to the surrounding mudrocks and causes the convergence of sand pressures and the least-principal stress.

Pre-existing fractures in the top seal of the crest are opened when pore pressures equal the least-principal stress (Hubbert and Willis, 1972). This increase in vertical fracture permeability induces fluid migration which continues until pore pressures fall below the least principal stress and the cap rock re-seals (Cathles and Smith, 1983).

This episodic fluid expulsion limits pore pressures to the least-principal stress at the 'leak-point' and can protect offset, hydraulically connected reservoir volumes by maintaining effective stresses at their subsidiary crests creating protected-traps (Lupa et al., 2002).

In this study, we elaborate upon the role of a minibasin leak-point in dynamically controlling the sand pressures, hydrocarbon trap integrities, and the flux of fluids to an overlying seafloor expulsion feature. We also propose a simple concept for employing leak-points as indicators of potential protected-trap hydrocarbon reserves.

## **2.2. Structure and Geology of the Popeye-Genesis minibasin**

The Popeye-Genesis minibasin is located in 2000 ft - 2900 ft (610 m – 880 m) water depth (Fig. 1a). The north-south oriented Genesis Ridge, which intersects the southward dipping seafloor (Fig. 1a), is the bathymetric expression of a salt-cored high that forms the western boundary of the Popeye-Genesis minibasin (Fig. 2b). The reservoirs within the Popeye-Genesis minibasin are bounded to the west and south by the salt-cored high, to the north by a regional growth fault, and to the east by a salt diapir (Figs. 2a and 2b).

Gas is trapped in the G-sand at the Popeye Field (GC72, 73, 116 and 117) and oil is trapped in the underlying H/N-sands at the Genesis Field (GC160, 161 and 205) (Figs. 2a, 2b and 3). The sands have bowl-like, elliptical geometries that are longer in the north-south direction (10.6 miles or 17 km) than in the east-west direction (5 miles or 8 km) (Figs. 2b and 3). The Popeye/Genesis sands record the proximal part of a larger sediment fairway that has existed for the last 5 m.y. (Rowan, 1995; Rowan and Weimer, 1998).

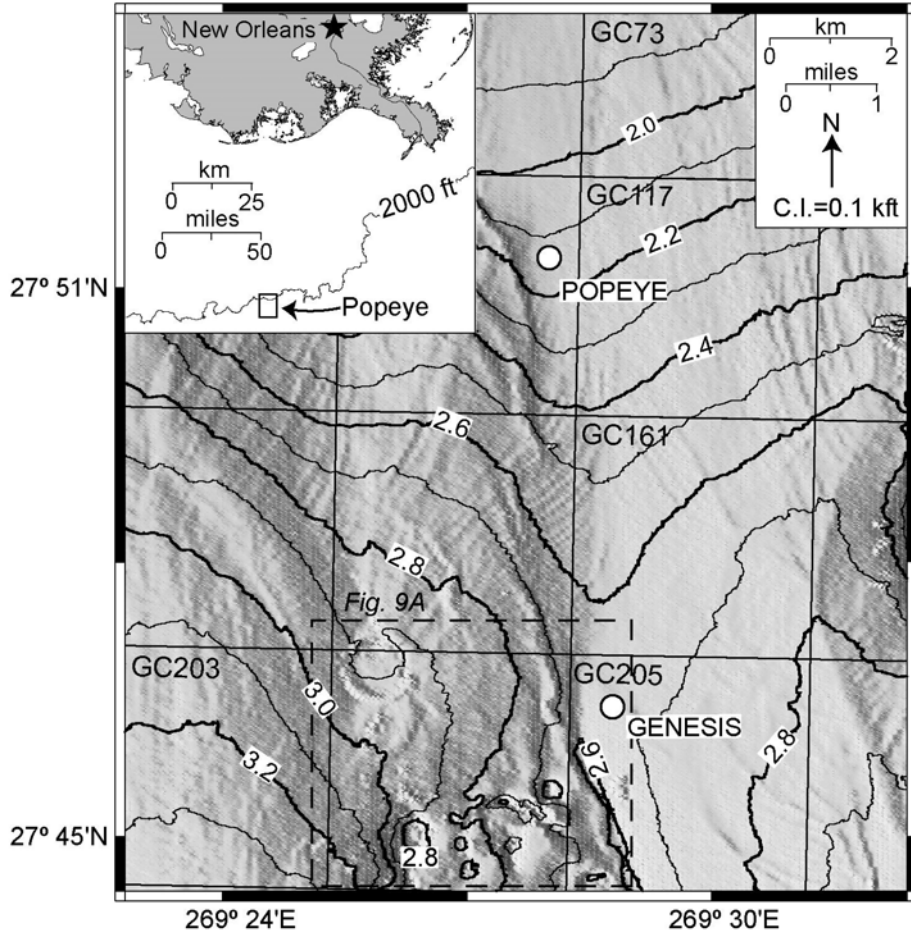


**Figure 1:** The Popeye-Genesis minibasin is located 140 miles southwest of New Orleans, offshore Gulf of Mexico. The sidelit bathymetry, mapped from 3-D seismic, displays a series of conical structures in GC204 that are interpreted to be expulsion features. An expanded view of the features in the dashed box is shown in Figure 10a. Black lines mark the boundaries of Green Canyon OCS blocks.

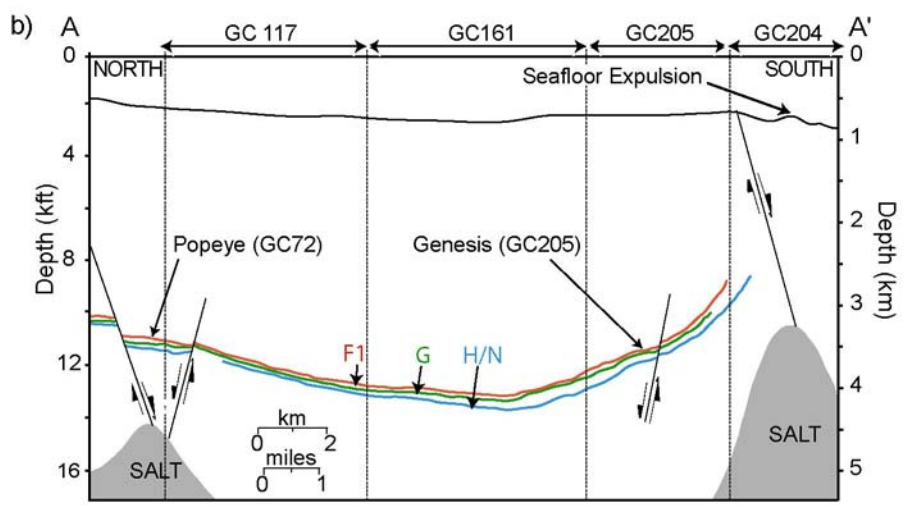
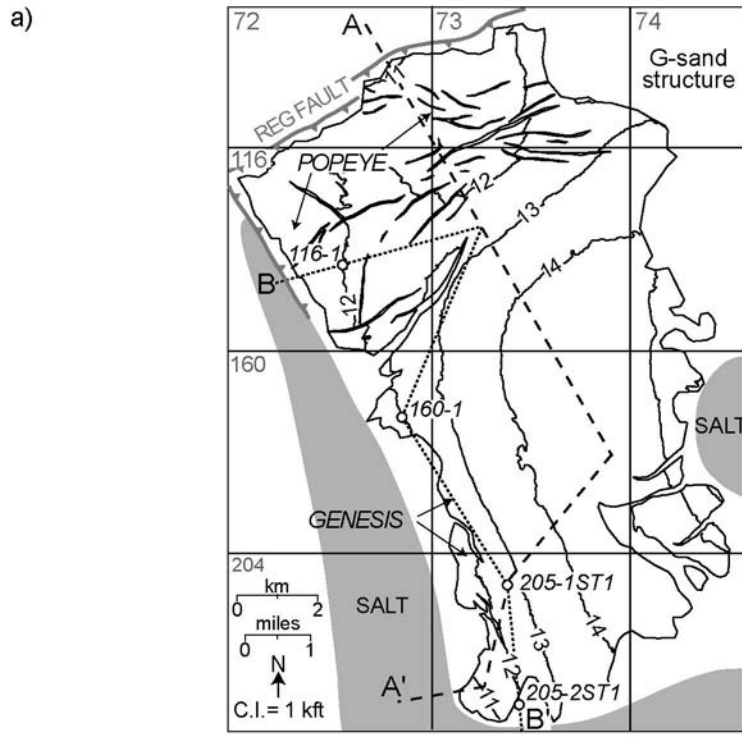


**Figure 2a:** Depth structure to the top of the G-sand with key minibasin bounding features in grayscale. Cross sections A-A' (Figs. 2b and 8b) and B-B' (Fig. 5) and the Popeye and Genesis fields are annotated. The depth conversion procedure used to create all structure maps (Figs. 2a, 3, 4 and 8d) is described in 2.2.1. **2b:** Structural cross section A-A' illustrates the synclinal geometry of the reservoir sands and structural traps of the two hydrocarbon accumulations.

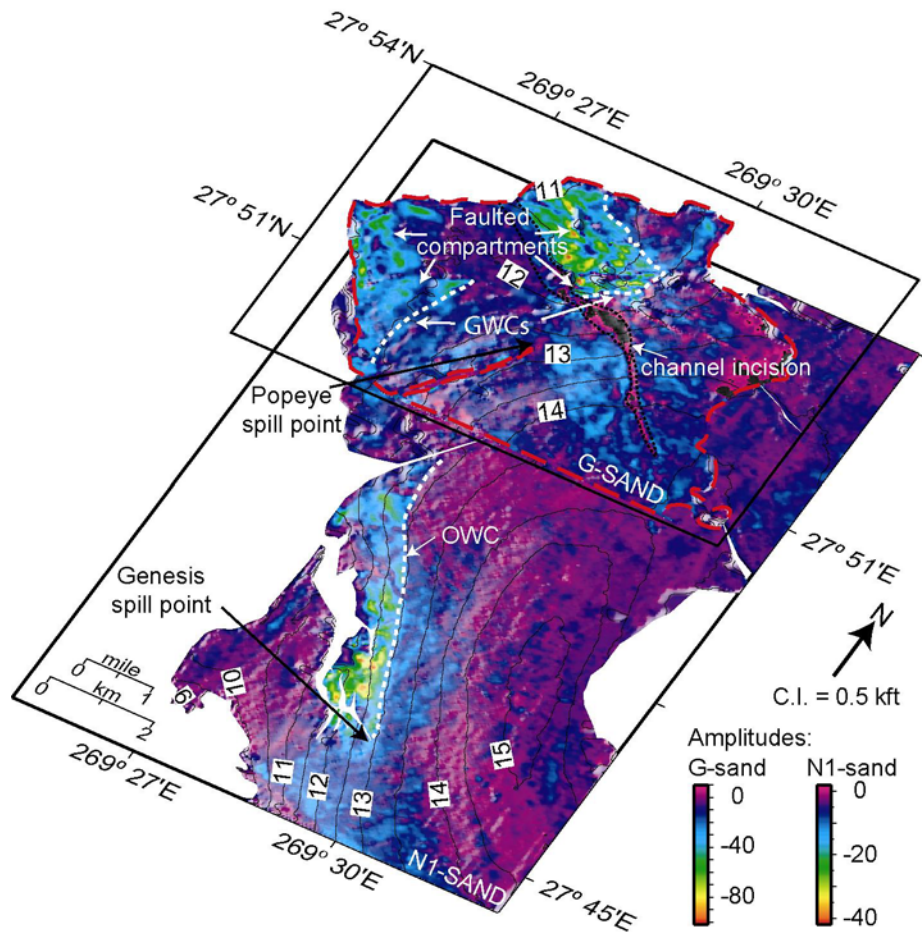


**Figure 3:** G- and N1-sand seismic amplitudes extracted at the trough-minima and overlain with depth contours. The G-sand horizon (gas saturated at Popeye) has been cropped to the south and located over the N1-sand (oil filled at Genesis) to demonstrate the relative location of hydrocarbons (bright amplitudes) in the minibasin.

### 2.2.1. Reservoir characterization and Depositional Setting

Structure maps of the H/N-, G-, and F1-sands were constructed across the minibasin from 3D seismic and well data (Fig. 4). At the margins of the minibasin, the sandstones thin and cannot be resolved on seismic data; this resolution limit is mapped as the spatial limit of the sandstone bodies (Fig. 4). The data upon which the maps are based are depth-converted using average sediment velocities. These velocities are

derived from well logs and are generally proportional to the two-way-time from the seafloor; velocity variation away from well control is contoured parallel to structure to reflect this increasing-velocity-with-depth trend. Lateral velocity variations between the Genesis field and the sand crests and a gas wipe out zone in the southwest of the minibasin (discussed later) are a significant source of potential errors in the depth conversion (Fig 4). The lateral velocity variation error is estimated by scaling the difference in sediment velocities from similar sub seafloor depths in the Genesis and Popeye fields to the lateral offset between the fields (5.6 miles or 9 km). This approach suggests lateral variation in velocity between Genesis and the sand crests to the southwest could result in a 400 ft (120 m) error.

The N-sand series are the most significant producing units of the Genesis field and the deepest in this study. Rafalowski et al. (1994) interpreted the N-sands as channelized turbidite deposits oriented to the southwest, parallel to the central high (Figs. 4c and 5). The N-sands have the broadest spatial distribution of the reservoirs, extending from Popeye in the north, where they correlate to the H-sands (Yuvancic-Strickland et al., 2003), over the Genesis high to the southern limit of the seismic data (Fig. 4c). They are thickest to the southwest (Fig. 5) suggesting there was greater accommodation space in this location during N/H deposition. Channel erosion prior to or coeval with the overlying G-sand deposition removed a portion of the N-sands in Block 117 (Fig. 4c). The crest of the H/N sandstone is at 8620 ft (2629 m) (Fig 4c, Table 1).

The G-sand overlies the N-sands. It is thickest at Popeye, thins to the southwest, and is not present over the Genesis high (Fig 4b). Yuvancic-Strickland et al. (2003) interpreted the massive base of the G-sand to be a sheet sand turbidite deposit and the overlying, laminated facies to be levee-overbank deposits (Fig. 5). G-sand may have been confined to the Popeye region through limited local accommodation space or

limited sand supply at the time of deposition. The crest of the G sandstone is at 10,200 ft (3100 m), significantly deeper than the crest of the underlying H/N sandstone (Fig. 4, Table 1).

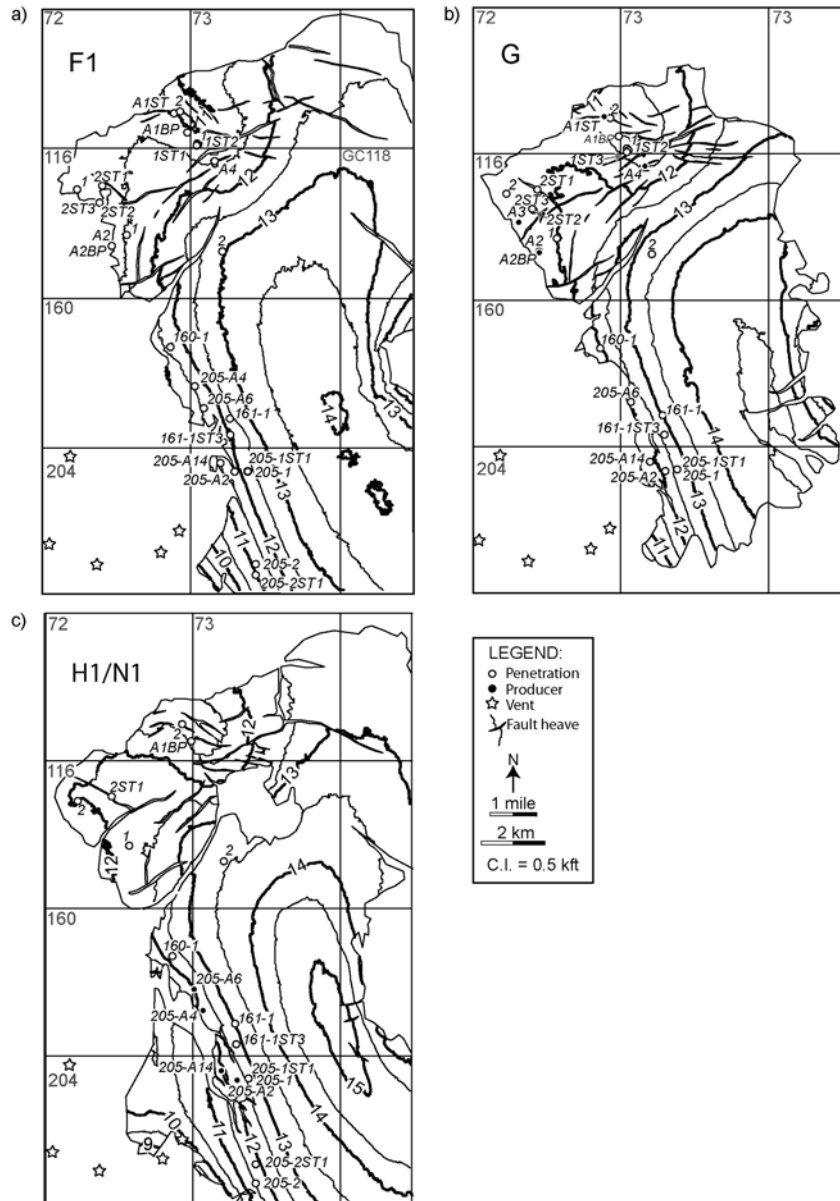


**Figure 4:** Sand structure maps of vertical depth to the top of the: **4a:** F1-sand, **4b:** G-sand and **4c:** N1-sand. The locations of seafloor expulsion features are annotated. Black and white circles mark the intersection of producing and exploration well paths with the displayed horizon. Well names do not include block numbers unless the wellpath-horizon intersection is outside the block.

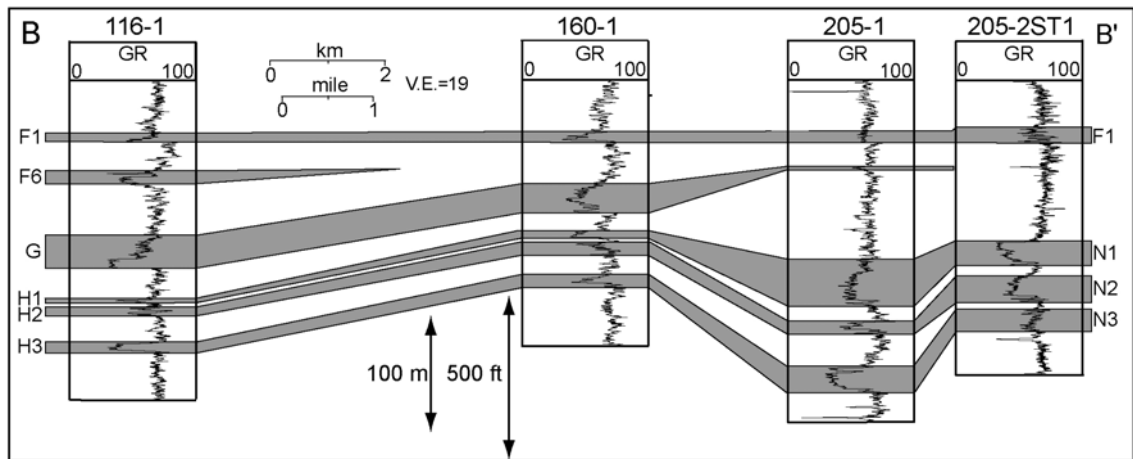


**Figure 5:** Correlated well log section from a north-south transect of the minibasin flattened to the base of the F1-sand (located on Fig. 2a). Sands are correlated by gamma-ray (GR) logs signatures at key well locations.

**Table 1:** Estimated overpressures and overburdens

Location	Sand	Contact (ft)	minibasin Crest (ft)	P (psi)	P <sub>w</sub> <sup>*</sup> (psi)	Sv @ crests	
						TVDSS (ft)	Sv (psi)
Expulsion	F1	-	8829	6822	2784	8829	6606
Expulsion	G	11795	10184	7236	2567	10184	8111
Expulsion	N1	12950	8625	6277	2320	8625	6989
Expulsion	N3	13199	9869	6277	2291	9869	7720

The F1-sand is present from Popeye in the north and is mapped to the southern limit of the data (Fig. 4a). Log signatures are of fining upward sheet sands of consistent thickness with variable mud content and blocky to serrate character (Fig 5). At Popeye and Genesis, the F1- and G-sands are separated by over 200 ft (60 m) of increasingly radioactive sediments topped by marls (Fig. 5). Prather et al. (1998) interpreted a

similar facies succession of draping hemipelagics as evidence of sediment starving during sea-level rise and potential healing of local depositional bathymetry to its equilibrium level. The crest of the F sandstone is at 8830 ft (2690 m) feet, slightly deeper than the crest of the N1-sandstone (Fig. 4a, Table 1).

## **2.3. Pressure, Stress and Trap Integrity**

### **2.3.1. Principal Stresses**

In passive margin settings, the overburden is generally assumed to be the maximum-principal stress ( $\sigma_v$ ) and consequently the least-principal stress is oriented horizontally ( $\sigma_h$ ) (Turcotte and Schubert, 2002). The overburden stress ( $\sigma_v$ ) is estimated by integrating the bulk density from wireline density logs (APPENDIX A). The estimated the overburden at Genesis is 350 psi (2.4 MPa) less than at Popeye because the water depth is 700 ft (215 m) greater (Fig. 6).

The least principal stress ( $\sigma_h$ ) is estimated from leak off tests (LOT), which are taken when drilling out of a new casing string (Table 2) (Fig. 6). Successful LOTs record the pressure value at which fluid flows into the formation through the opening of formation fractures. These measurements record an upper bound of the least-principal stress because they may include hoop stress effects or the effects of formation strength (Hubbert and Willis, 1972). At both fields, the least-principal stress is extremely close to the overburden ( $\sigma_h / \sigma_v \geq 0.95$ ) (Table 2), which indicates that the stress state is nearly isotropic. Lupa (2002) found similar behavior at the Bullwinkle Field with ( $\sigma_h / \sigma_v \geq 0.975$ ). A linear regression of the LOT data vs depth is used to estimate the least principle stress at any depth (Fig. 6, dashed line).

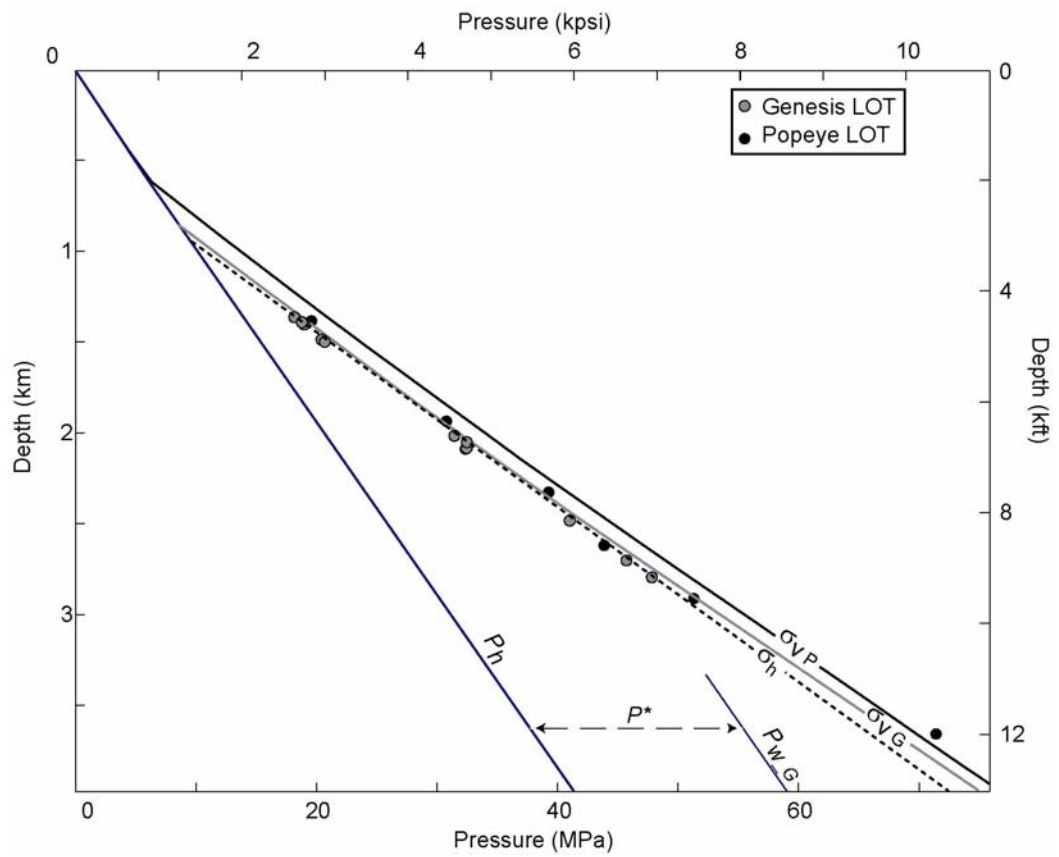


**Figure 6:** Bounding stresses plot showing the hydrostatic pressure ( $P_h$ ), overburden stresses ( $\sigma_{VP/G}$ ) and least-principal horizontal stress ( $\sigma_h$ ). The G-sand aquifer ( $P_{w,G}$ ) pressure is plotted to illustrate overpressured ( $P^*$ ) nature of the minibasin aquifers.

**Table 2:** LOT data summary

<b>Wellname</b>	<b>TVDSS (ft)</b>	<b>LOT (psi)</b>	<b>Sv (psi)</b>	<b>Sv-LOT (psi)</b>	<b>Normalized LOT/Sv</b>
117-A4	4265	2755	2871	116	0.96
117-A4	6331	4466	4742	276	0.94
117-A4	7615	5699	5945	246	0.96
117-A4	9528	7439	7772	333	0.96
117-2	4514	2842	3089	247	0.92
117-2	6821	4684	5191	505	0.90
117-2	8550	6351	6815	464	0.93
117-2	11982	10368	10150	-218	1.02
<b>Popeye Average</b>				<b>247</b>	<b>0.95</b>
161-1	4491	2712	2828	116	0.96
161-1	6778	4742	4901	159	0.97
161-1	9154	6975	7105	130	0.98
205-2	4442	2639	2784	145	0.95
205-2	4518	2741	2857	116	0.96
205-2	8091	5989	6105	116	0.98
205-2	8812	6685	6786	101	0.99
205-2	8845	6670	6815	145	0.98
205-A2	4806	2987	3103	116	0.96
205-A14	4862	3045	3161	116	0.96
205-A14	6588	4597	4713	116	0.97
205-A14	6703	4713	4829	116	0.98
<b>Genesis Average</b>				<b>131</b>	<b>0.97</b>

### 2.3.2. Reservoir Pressures

We review the extrapolation of reservoir pressures for the N1-sand. A Repeat Formation Test (RFT) measured the N1-sand pre-production formation pressure within the oil column at Genesis (8243 psi at 12776 ft) (Fig. 7c, white circle) (Table 3). This pressure is extrapolated down a static oil gradient (Table 4) to the seismically defined oil-water contact (OWC) (Fig. 3) (Fig. 7c, solid-thick line). At the OWC (8288 psi at 12950) ft, the oil pressure ( $P_o$ ) is assumed to equal the water pressure ( $P_w$ ).

The water phase pressure is then extrapolated from the OWC along a hydrostatic gradient (Table 4) up to the sand crest (8620 ft, 2630 m) and down to the synclinal low (15200 ft, 4630 m) (Fig. 8a). In this manner, the water phase pressure ( $P_w$ ) is predicted everywhere within the minibasin. The water-phase overpressure:

$$P_w^* = P_w - P_h \quad (1)$$

(2300 psi, 15.9 MPa) is a useful way to characterize and compare the sandstone pressures because it is independent of depth (Fig. 7c).

This extrapolation hinges on the assumption that the fluid pressures follow their respective static gradients and that the hydrocarbon pressures equal the water pressures at the hydrocarbon-water contact. For the pressures to follow their static gradients the permeabilities must be high relative to any flow rate being applied. This is consistent with the 235 to 3000 md core sampled permeabilities from the Popeye and Genesis reservoir sands and down dip reservoir continuity interpreted along the strike of the Genesis field from fluid sample comparisons (Rafalowski et al., 1994; Beeunas et al., 1999; Yuvancic-Strickland et al., 2003). In addition, for the hydrocarbon phase pressure to equal the water phase pressure at the hydrocarbon-water contact, the sand must

have relatively large pore throats resulting in a low capillary entry pressure. Analysis of G-sand cores suggests that the capillary entry pressure is only 5 psi.

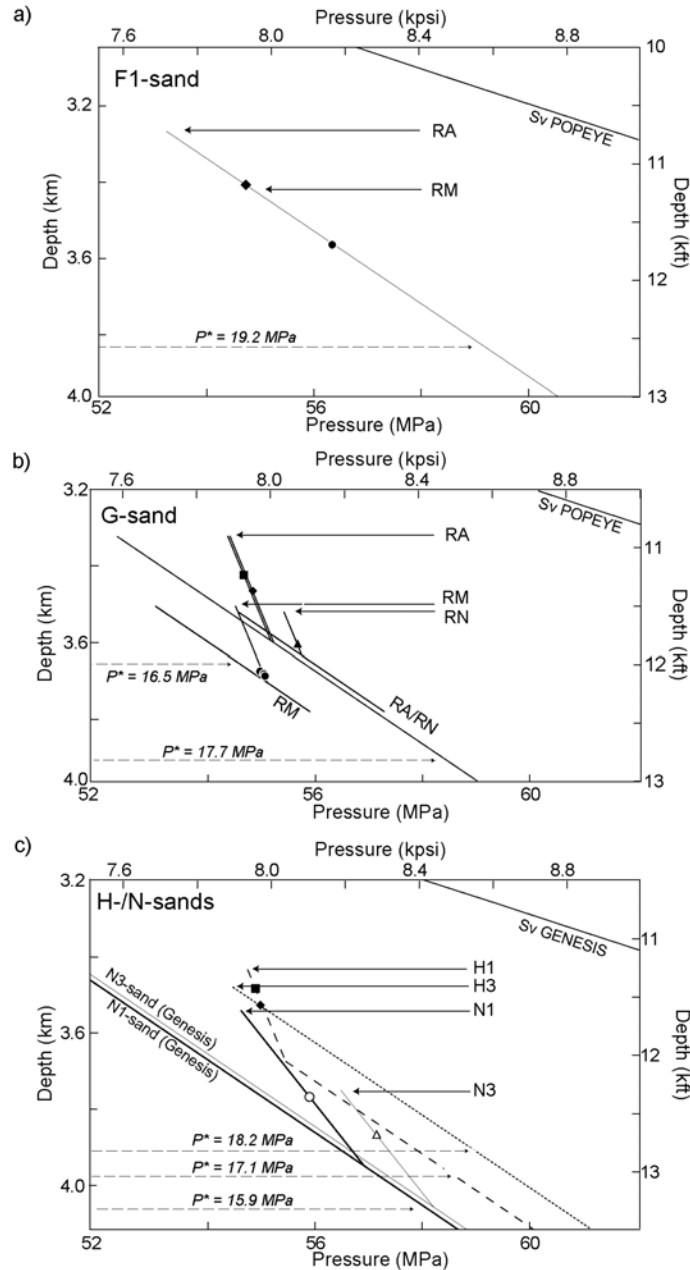


**Figure 7:** Pressure-depth plots defining aquifer pressures through extrapolation of RFT data for the **a:** F1-sand, **b:** G-sand and **c:** H- (Popeye) and N-sand (Genesis). Shapes differentiate between specific pre-production RFTs from Popeye (black) and Genesis (white) fields respectively. Calculated overpressures for each sand are annotated.

**Table 3:** RFT data and structural summary

Location	Sand	Fluid	RFT (psi)	RFT (m)	Contact (psi)	Contact (m)	Field Crest (m)	P <sub>w</sub> * (psi)
Popeye	F1	Water	7932	11184	-	-	10810	2784
Popeye	G	Gas	7923	11234	7997	11795	10856	2567
Popeye	H1	Gas	7955	11424	8111	12051	11263	2639
Popeye	H3	Water	7966	11476	-	-	11099	2480
Genesis	N1	Oil	8243	12776	8288	12950	10997	2320
Genesis	N3	Oil	8416	13048	8456	13199	12303	2291

**Table 4:** Fluid density gradients

Fluid	Gradient	
	psi/ft	MPa/km
Water column	0.444	10.05
Water within sediment column	0.465	10.52
Oil	0.25	5.66
Gas	0.13	2.94

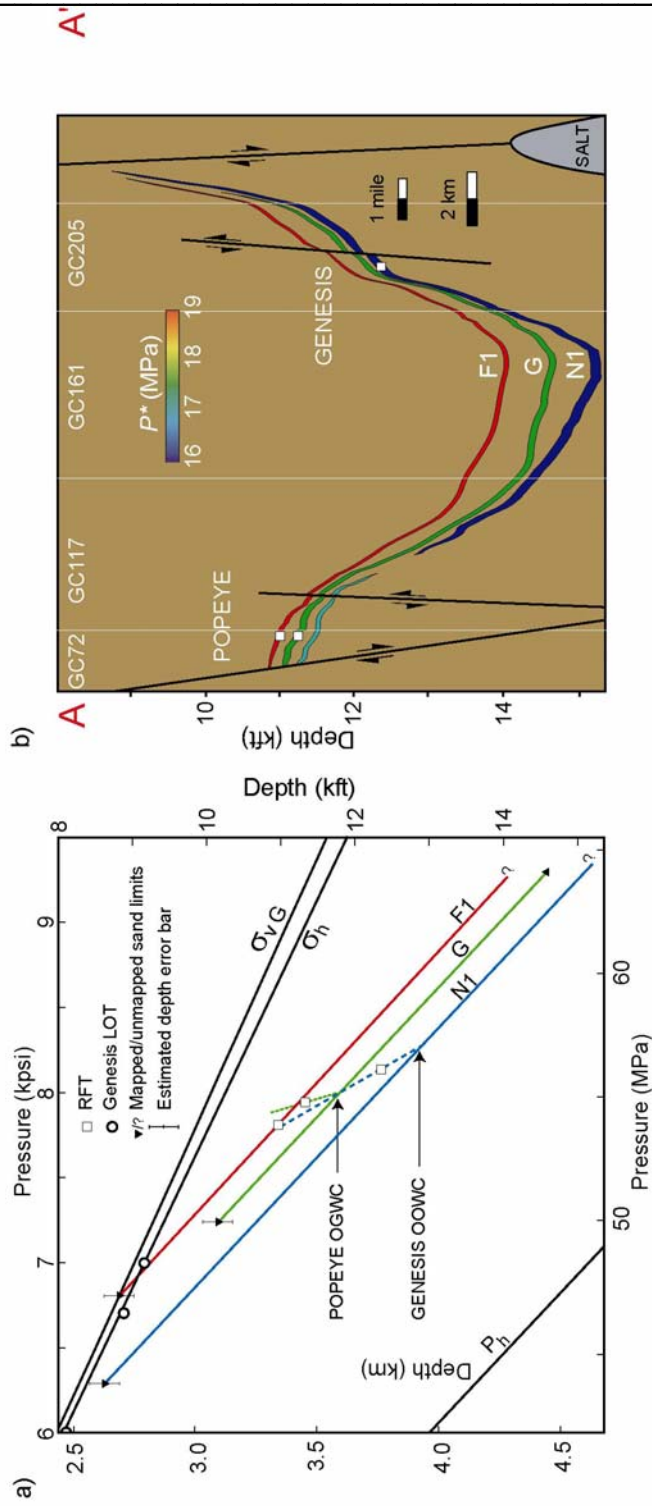


**Figure 8a:** Minibasin scale pressure-depth plot illustrating the convergence of the pore pressures of the F1- and N1-sands with the least-principal stress. Vertical bars at the sand crests express the estimated errors inherent from the depth conversion of seismic horizons. **8b:** Structural cross section A-A' paralleling the adjacent pressure depth plot and emphasizing the counter-intuitive aquifer overpressure distribution within the minibasin. Sand thicknesses are exaggerated for display purposes; hydrocarbon fill is ignored (located on Fig. 2a).

Two different G-sand overpressures are present at Popeye: 2570 psi (17.7 MPa) in the RA and RN reservoir and 2400 psi (16.5 MPa) in the RM reservoir (Fig. 7b). We doubt the quality of the RFTs for the RM overpressure because they do not follow the gas gradient (Fig. 7b). Yuvancic-Strickland et al. (2003) describe the compartmentalization in the G-sand at Popeye and interpret that the G-sand RM/RN pressures are transmitted downdip from Popeye through the minibasin aquifer (Fig. 4b). Finally, the F1-sand overpressure of 2784 psi (19.2 MPa) is defined by independent RFTs at Popeye (Fig. 8a).

### 2.3.3. Definition of a Minibasin Leak-point

The shallowest location for each of the reservoir sandstones is in the southwest corner of the minibasin in Blocks 204 or 205 (Fig. 4). At this crestal location both the F1- and N1-sand pore pressures approximate the least-principal stress ( $\sigma_h$ ); the F1 is slightly higher and the N1 pressure is slightly lower (Fig. 8a, Table 1). As a result, the horizontal effective stress ( $\sigma'_h$ ):

$$\sigma'_h = \sigma_h - P_p \quad (2)$$

is approximately zero  $\sigma_h$  in both locations. Finkbeiner et al. (2001) reviewed two processes whereby permeability is increased at low effective stresses: 1) hydraulic fracturing at zero (Hubbert and Willis, 1972); or 2) coulomb frictional failure along pre-existing faults at low, but non-zero, effective stress (Barton et al., 1995). Despite the potential error in our estimates of the sand depth and effective stress state we suggest that crestal pore pressures are great enough to open hydraulic fractures in the cap rock and induce fluid expulsion. We term this location the minibasin leak-point.

The minibasin leak-point causes an unusual pressure distribution whereby the F1-sand overpressure is greater than the deeper N1-sand overpressure (Fig. 8b). The

crest of the N1-sand is shallower than the crest of the F1-sand (Fig. 8b). As the pore pressure at both crests approaches the least-principal stress the N1 leak-point is therefore at a lower pressure than the F1-leak-point (Fig 8a). The model is akin to a tea kettle boiling: pressure builds up beneath the crest until it reaches a critical pressure that equals the least principal stress of the overlying rock; thereafter the fluid migrates vertically through the cap rock and no further pressure can be built up.

The G-sand is not leaking fluid at its crest is at a stable effective stress. However, it is sandwiched between the overlying, higher pressured, F1 sandstone and the underlying, lower pressured, N1 sandstone; as a result it has an equilibrated immediate pressure.

#### **2.4. Seafloor Expulsion System**

The leak-point of the N1-sand is overlain by a zone of chaotic, low amplitude reflectors (Fig. 9c). Brooks et al. (1986) mapped this 'gas wipeout zone' (GWZ) through GC204, 247 and 248 (south of this seismic dataset).

Spectacular seafloor expulsion features are present above the GWZ (Figs. 9a and 9b). Two symmetric mounds in the northwest and south center of GC204 (Locations 1 and 3) overlie discrete, vertical GWZs which mask underlying reflectors (Figs. 9a, 9c and 9d). Location 1 is a shallow (50 ft, 15 m relief), wide (3300 ft, 1 km in diameter) mound; this contrasts the steep (160 ft, 50 m relief), narrow cone (1400 ft, 425 m in diameter) at Location 3 (Fig. 9a). The seafloor-seismic amplitudes over these mounds are four to eight times the magnitude of the equivalent surrounding seafloor muds (Locations 1 and 3, Fig. 9a). Flow-like features, delineated by slightly dimmer amplitudes (Location 2), emanate from these conical mounds in a radial pattern. Away

from the mounds they rotate down the bathymetric slope to the south, extending laterally to the limit of the seismic dataset (over 6 km) (Fig. 9a).

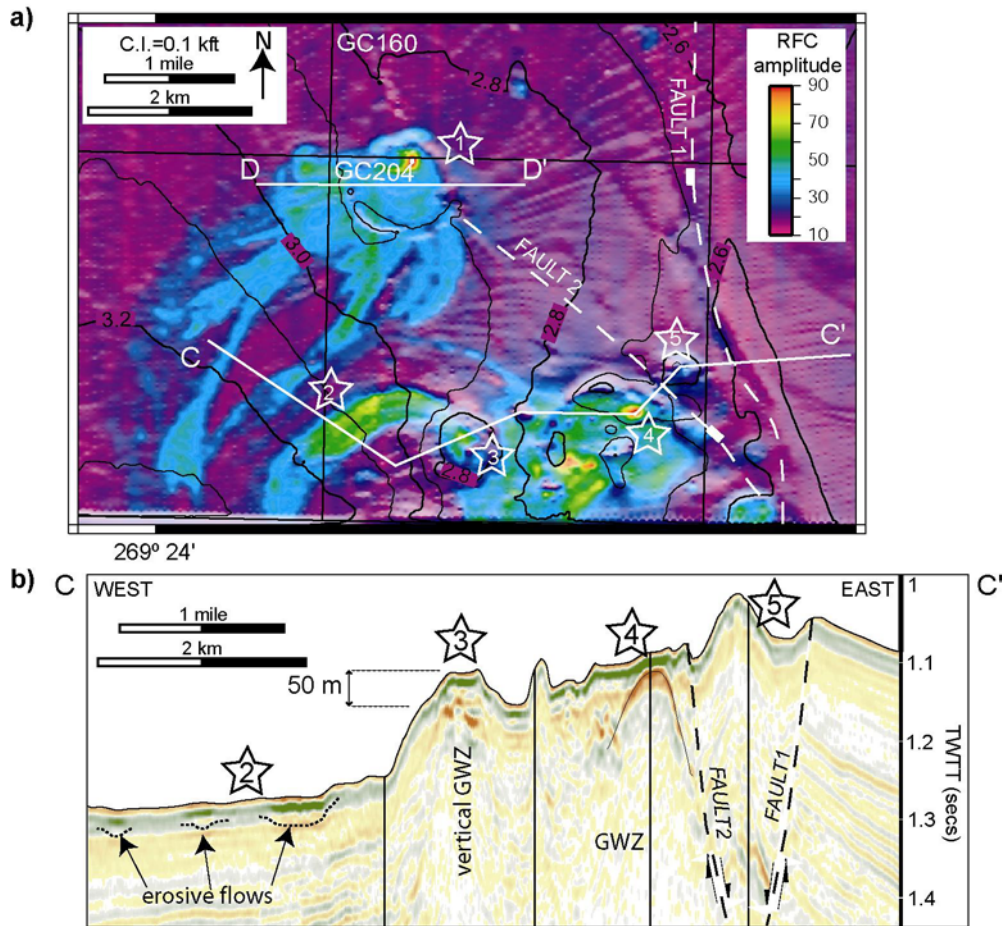


**Figure 9a):** Amplitude extraction of the seafloor seismic horizon 'maxima' over the block GC204 with bathymetric contours overlain (located on Fig. 1). Structures distinct from the surrounding seafloor (stars 1-5) and their characterizing cross sections C-C', D-D' are annotated. **9b):** Shallow-time, seismic cross section C-C' comparing amplitude magnitude to bathymetric structure (located on Fig. 9a). Locations 1 (see Fig. 9d) and 3 (mud volcanos) and locations 3, 4 and 5 (mud cones and hydrocarbon seeps) are believed to represent separate systems.

The remainder of the seafloor features form a composite high to the east of Location 3; two types of structure are present exemplified at Locations 4 and 5. Location

4 typifies low relief areas of mottled, bright amplitudes up to 10 times those of the surrounding mud (Fig. 9a). These bright amplitudes are bounded by lower-amplitude, high-relief structures (Location 5). Both structures source significantly smaller flow features than Locations 1 and 3 although it is possible additional flows are present south of the study area (Fig. 9a).

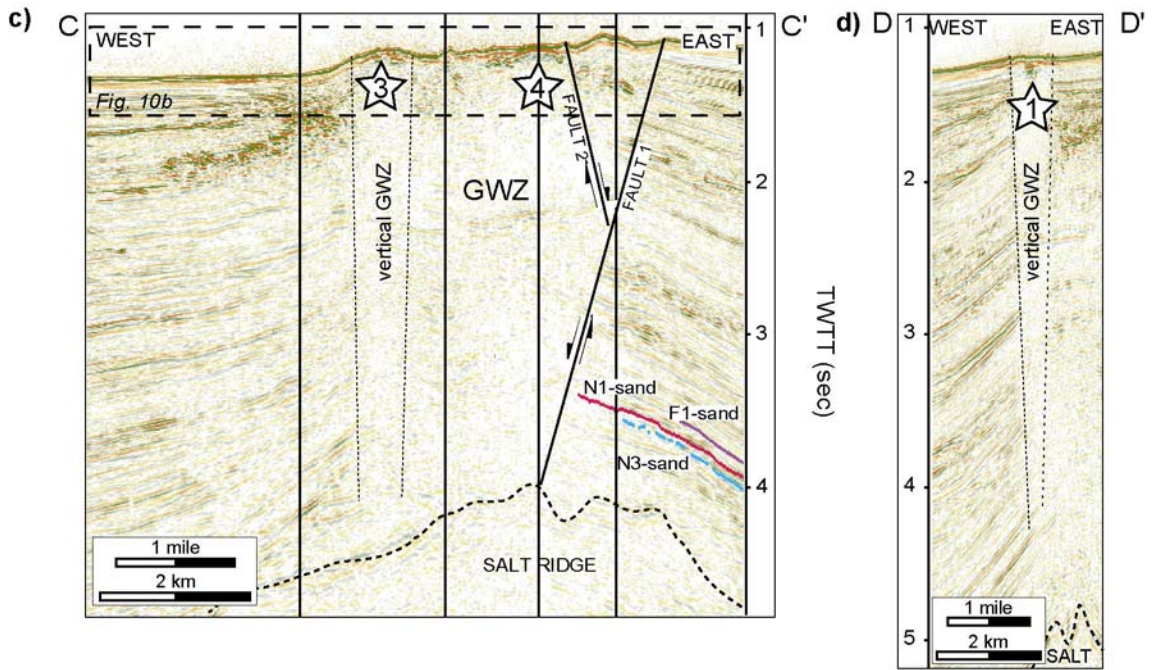


**Figure 9c):** Seismic cross section C-C' illustrates the proximity of the sand crests, salt related faulting and overlying seafloor expulsion features (located on Fig. 9a). **9d):** Seismic cross section D-D' illustrates the deep time structure of the northern mud volcano; note the vertical expulsion pathway

Two studies have sampled the Genesis expulsion features. Brooks et al. (1986) mapped the GWZ using shallow 2-D seismic data and piston cores. Structure II gas hydrates, ice like compounds of hydrocarbons ( $C_1-C_4$ ) trapped in a rigid water lattice, were recovered close to Location 4 and sporadically over the GWZ (Fig. 9a). The larger molecular content of these thermogenic hydrates indicates they are products of deeper petroleum systems (Sassen et al., 2001). Boettcher and Abrams (2000) also sampled

the Genesis expulsion structures with a submersible, defining areas of active (bacterial mats, live clams and oil and gas saturation) and relict (carbonate blocks, dead clams and mud mounds) seepage. Oil samples collected from active seeps had similar molecular characteristics to oils in the N-sand series at Genesis (Boettcher and Abrams, 2000).

Locations 1 and 3 are interpreted to be mud volcanoes exhibiting many features similar to those described in prior studies. Key features include a conical geometry produced by accumulation of extruded material (Fig. 9a) (Neurauter and Bryant, 1990; Milkov, 2000) and vertical, subsurface feeder systems (vertical GWZ) (Figs. 9c and 9d) (Roberts et al., 2001; Yin et al., 2003). The amplitude supported flows at Location 2 represent the expelled products of the mud volcanoes; these were sampled on a submersible dive and found to contain highly consolidated mud breccia (Fig. 9a) (Boettcher, 2003). The depth of exhumation of the expulsion source is unknown; however foraminifera dated between 3 and 3.9 Ma have been sampled at similar mud volcanoes 60 miles to the west (CC272) (Kohl and Roberts, 1994).

The composite high adjacent to Location 3 is dominated by relict mud volcanoes and localized hydrocarbon seeps associated with underlying gas hydrates. The inactivity of the mud volcanoes (typified by Location 5) is interpreted from the relatively dim amplitudes and lack of flow features (Fig. 9a). These structures also lack the distinct vertical GWZs present beneath Locations 1 and 3 and are presumably sourced by the underlying fault system (Fig. 9b) (Boettcher and Abrams, 2000). The abrupt transition of seafloor amplitudes observed at Location 4 is typical of gas hydrate accumulations (Roberts and Carney, 1997) (Fig. 9a). The high reflectivity has been shown at similar features to occur over well defined zones of seafloor lithification and outcropping gas hydrate (Roberts and Carney, 1997). The lithification is produced by

authigenic precipitation of carbonates from the bacterial degradation of crude oil and gas (Ritger et al., 1987; Roberts and Aharon, 1994).

The morphological characteristics of the mud volcanoes and gas hydrate locations may indicate two fluid flow systems. Boettcher and Abrams (2000) noted that flux varied greatly between major expulsion features and proposed that a background slow seepage through the area is punctuated by periods of episodic venting. Episodic venting is consistent with the transient nature of the mud volcano flows (Fig. 9a), and the steady, slow seepage is evidenced by the presence of gas hydrates which require a prolific, super-saturated source in a dynamic seafloor location (Egorov et al., 1999).

We propose that the N1-sand leak-point contributes fluids to these gas hydrates via the overlying active fault system. Fault plane migration is consistent with the preservation of reflections to the east of this fault plane (FAULT 1), directly overlying the leak-point, and the GWZ present to the west of the fault plane (Fig. 9c).

## **2.5. Discussions and applications**

Fluid expulsion from the crests of the F1- and N1-sands (minibasin leak-point) constrains the pore pressures and hydrocarbon trap integrities of the minibasin sands. Fluids also contribute to the overlying Genesis seafloor expulsion features (Fig. 10).

Through the extrapolation of reservoir pressures we observe that the shallower F1-sand has a greater aquifer pressure than the deeper N1-sand at the same depth; the G-sand lies stratigraphically between the two and has an intermediate pressure (Fig. 10b). This unusual decreasing-overpressure-with-depth relationship is created by the shallower location of the N1 leak-point relative to the F1 leak-point (Fig. 10a, Table 1). Pore pressures at both leak-points intersect the same least-principal stress curve and so

despite it being stratigraphically deeper position the N1-sand is defined with a lower overpressure (Fig. 10b).

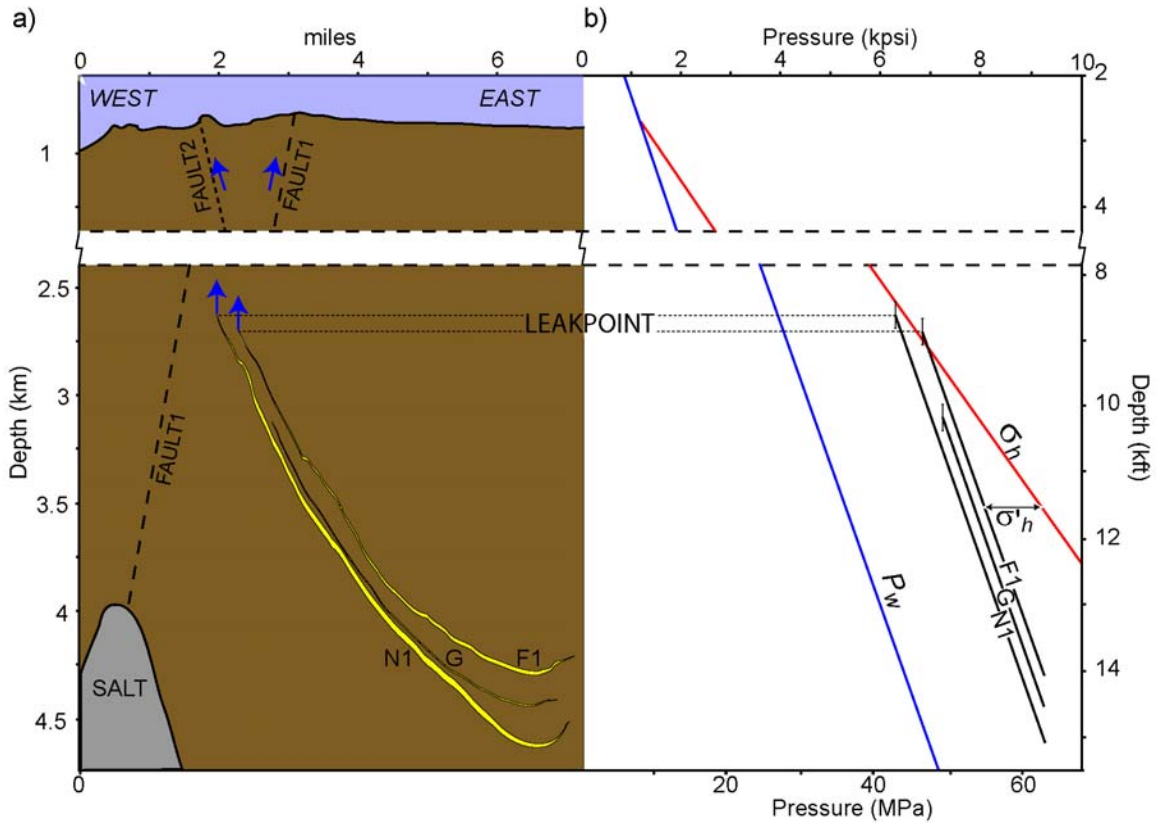


**Figure 10:** Geologic cartoon and parallel pressure depth plot summarizing **a)** the influences of the sand crest failure on the control of the minibasin pressure profile and **b)** flux of fluids to the seafloor expulsion features.

We conjecture that pore pressures are limited to the least-principal stress by fluid expulsion at zero effective stresses (Equation 2) when pre-existing fractures in the cap rock dilate and fluid migrates from the sand crest. Fluid expulsion continues until pressures deplete and fall below the least-principal stress. This fracturing and re-sealing becomes cyclic if the sand crest experiences a consistent increase in pore pressures

through time, either through migrating hydrocarbons and/or increasing overpressures (Cathles and Smith, 1983). This cyclic expulsion effectively equilibrates the sand crest pressures to the least-principal stress (Fig. 10a).

Two insights result from this pressure-stress equilibration at the leak-point: 1) the trap integrity of hydrocarbon accumulations within the sands at greater effective stresses are protected, and 2) by realizing this equilibration point we can estimate the protected trap integrities of exploration targets associated with fluid expulsion without direct pressure data.

Protection of the N1-hydrocarbon trap is illustrated by considering a reduction in the effective stress of the system. This can be achieved by increasing the sand overpressure or reducing the least-principal stress and will result in fluid expulsion until the aquifer system ( $P_w$ ) is re-equilibrated with the least-principal stress (Fig. 11a). The effective stress state of the hydrocarbon trap is directly linked with this equilibration and so the trap integrity ( $\sigma'_{hTRAP}$ ) is intrinsically protected (Fig. 11a).

The concept of protection of subsidiary structures through fluid expulsion is useful. By assuming equilibration of leak-point pore pressures and the least-principal stress we can reverse extrapolate from the leak-point to the subsidiary trap crest providing a simple 'quick look' estimate of the trap integrity. This method does not require direct pressure data from the sands and can be completed with an understanding of the depth structure and least-principal stress.

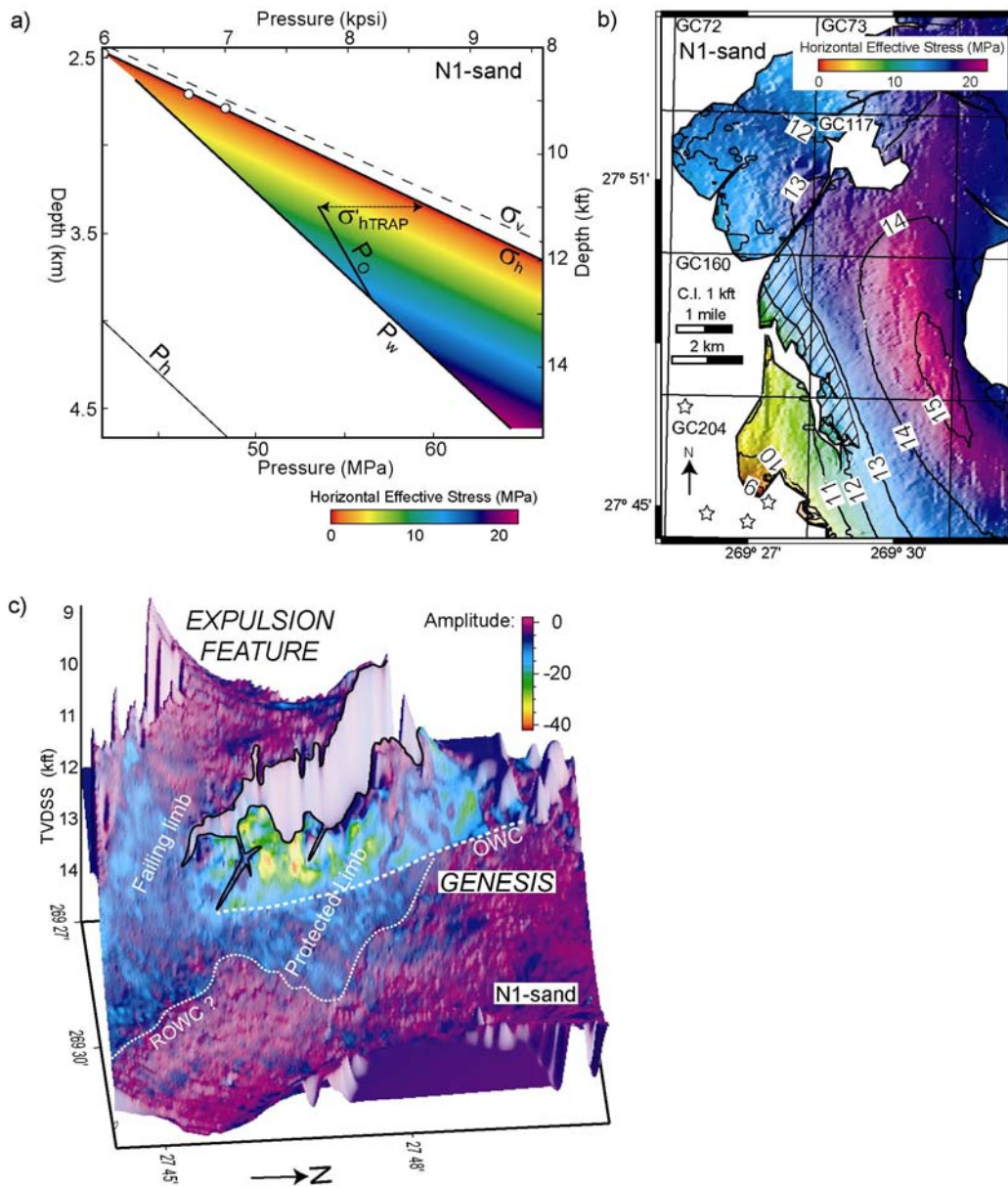


**Figure 11a:** Analyzing the variation in horizontal-effective stress at the leak-point for the N1-sand. The hydrocarbon trap has significantly greater effective stress than the sand crest. **11b:** Mapping the horizontal-effective stress across the N1-sand with TVDSS contours overlain. This image illustrates the susceptibility of sand to failure spatially identifying likely leak-points and protected traps (diagonal pattern). **11c:** 3-D image of the N1-sand structure with its amplitude extraction overlain shows that the protected limb is filled to the spill point. Bright aquifer values (residual amplitudes) in the failing limb of the sand indicate it has experienced hydrocarbon fill and has since failed protecting the reserves at Genesis.

We can improve our location and quantification of protected traps and leak-points by spatially mapping the horizontal-effective stress (Equation 2) across sand structure; this was completed for the N1-sand (Fig. 11b). Analysis in map view allows for the incorporation of changes in the least-principal stress that are not possible in the traditional pressure-depth plot (Fig. 11b). We assume least-principal stress behaves in a similar fashion to our extrapolated overburden (APPENDIX A) (Fig. 6).

Changes in least-principal stress from the point of original calculation (Genesis) are proportional to changes in water depth from the same location (no lateral change in sediment density). For this reason the effective stress does not exactly follow sand structure (Fig. 11b). The Genesis field bounding fault separates the deep, higher effective stresses (cooler colors) of the Genesis Field 'protected limb' from the lower effective stresses (warm colors) of the leak-point associated 'failing limb' within the N1-sand (Figs. 11b and 11c). The southern tip of this fault creates the structural closure for the subsidiary protected trap at Genesis (diagonal lines, Fig. 11b). In reality this protected limb is filled to this spill point with bright, large amplitudes clearly delineating an OWC parallel to structure (Fig. 11c).

The expulsion of fluids from this system is evidenced by an area of seismic amplitudes brighter than the average aquifer amplitude. These residual hydrocarbon amplitudes are present down dip of the OWC and orient up the failing limb to the interpreted leak-point (Fig. 11c). Hydrocarbon accumulation within the failing limb indicates the system was previously at greater effective stresses. The expulsion of this significant volume is potentially related to the opening of the Genesis fault system or increased overpressuring during burial. Sassen et al. (2003) interpret a late gas charge to the region through comparison of gas stored in the Genesis N-sands and gas venting at the seafloor 20 miles to the south. This late gas charge at or near the current burial

depth flushed the reservoirs displacing the original biodegraded gas (Sassen et al., 2003). This was presumably enough charge to create recent fluid expulsion at the leak-point sourcing significant volumes of fluids to the shallower seafloor system.

Fluids migrating from the deeper petroleum system would likely focus along an active fault plane (FAULT 1), adjacent to the minibasin leak-point. Boettcher and Abrams (2000) identified the seafloor expression of this fault system as the charge pathway for actively venting seeps and found fluids sampled at these seeps were molecularly similar to those stored in the N1-sand at Genesis.

## **2.6. Conclusions**

Hydrocarbon trap integrity at the Genesis and Popeye fields is protected by fluid expulsion at a leak-point in the southwest of the minibasin. Equilibration of N1-sand crest pressures with the least-principal stress at this leak-point protects the hydrocarbon trap integrity of the Genesis Field 3 miles (5 km) to the north. Similar failure F1-sand at a deeper location creates an unusual decreasing-pressure-with-depth profile. The G-sandstone has a deeper crest than both the F1- and N1-sandstones with pore pressures significantly lower than the least-principal stress; we infer pore pressures equilibrate between the overlying F1- and underlying N1-sands. In this manner fluid expulsion at the leak-point indirectly protects the trap integrity at Popeye 8 miles (13 km) to the north.

Physical evidence for fluid expulsion and contribution to the overlying seafloor features include a residual hydrocarbon seismic signature, an active migration pathway between the two systems, compositional similarities between fluids expelled at the seafloor and those produced from the Genesis field (Boettcher and Abrams, 2000) and a late gas charge story which corroborates a recent venting history (Sassen et al., 2003).

Trap protection by this leak-point equilibration process is used to suggest a simple methodology for the prediction of the location and integrity of protected traps in frontier exploration settings.

## 2.7. Appendix A: Estimation of Overburden Stresses

The overburden stress ( $\sigma_v$ ) was estimated between 2000 and 4400 feet at Popeye, where there was no bulk density logging data, by assuming an empirical porosity-effective stress relationship:

$$\phi = \phi_0 e^{-\beta(\sigma_v - P_h)} \quad , \quad (2)$$

where  $\phi$  is the porosity,  $\phi_0$  is the reference porosity,  $\beta$  is the compressibility,  $\sigma_v$  is the vertical stress, and  $P_h$  is the hydrostatic pressure (Rubey and Hubbert, 1959; Ham, 1966; Hart et al., 1995; Flemings et al., 2002). To calculate  $P_h$ , a water density ( $\rho_w$ ) of 1024 kg/m<sup>3</sup> (salinity = 35,000 ppm) was assumed whereas within the sediment column, a water density of 1070 kg/m<sup>3</sup> (salinity = 100,000 ppm) was assumed. The compressibility constant ( $\beta = 3.13 \times 10^{-2} \text{ MPa}^{-1}$ ) and reference porosity ( $\phi_0 = 0.42$ ) were defined by a log-linear regression of  $\phi$  vs  $\sigma_v$  with the shallowest wireline bulk density data available (between 4400 and 6000 feet) (e.g. Hart *et al.* (1995)). Elsewhere in the minibasin, (Genesis and the expulsion feature), density below the seafloor was assumed to vary with subsea depth in the same manner as at Popeye.

**Table 5:** Nomenclature

Variable	Description	Dimensions
$B$	Compressibility constant	$M^{-1}LT^2$
$g$	Acceleration due to gravity	$LT^{-2}$
$\phi$	Porosity	-
$\phi_0$	Reference Porosity	-
$P_p$	Pore Pressure	$ML^{-1}T^{-2}$
$P_w$	Water phase pressure	$ML^{-1}T^{-2}$
$P_o$	Oil phase pressure	$ML^{-1}T^{-2}$
$P_g$	Gas phase pressure	$ML^{-1}T^{-2}$
$P_h$	Hydrostatic pressure	$ML^{-1}T^{-2}$
$P^*$	Overpressure	$ML^{-1}T^{-2}$
$\rho_w$	Water/brine density	$ML^{-3}$
$\sigma_v$	Maximum vertical-principal stress	$ML^{-1}T^{-2}$
$\sigma_h$	Horizontal least-principal stress	$ML^{-1}T^{-2}$
$\sigma'_h$	Horizontal effective stress	$ML^{-1}T^{-2}$

## References

- Barton, C. A., M. D. Zoback, and D. Moos, 1995, Fluid flow along potentially active faults in crystalline rock: *Geology*, v. 23, p. 683-686.
- Beeunas, M. A., T. A. Hudson, J. A. Valley, W. Y. Clark, D. K. Baskin, and Anonymous, 1999, Reservoir continuity and architecture of the Genesis Field, Gulf of Mexico (Green Canyon 205); an integration of fluid geochemistry within the geologic and engineering framework, *AAPG Bulletin*, v. 83: Tulsa, American Association of Petroleum Geologists, p. 1348.
- Boettcher, S. S., 2003, Personal Communication.
- Boettcher, S. S., and M. A. Abrams, 2000, Mapping migration pathways using geophysical data, seabed core geochemistry and submersible observations in the central Gulf of Mexico: *NOGS Log*, v. 41, p. 7.
- Brooks, J. M., H. B. Cox, W. R. Bryant, M. C. Kennicutt, II, R. G. Mann, and T. J. McDonald, 1986, Association of gas hydrates and oil seepage in the Gulf of Mexico, *in* D. Leythaeuser, and J. Ruellkotter, eds., *Organic Geochemistry*, v. 10: Oxford-New York, Pergamon, p. 221-234.
- Cathles, L. M., and A. T. Smith, 1983, Thermal Constraints on the Formation of Mississippi Valley-Type Lead-Zinc Deposits and Their Implications for Episodic Basin Dewatering and Deposit Genesis: *Economic Geology*, v. 78, p. 983-1002.
- Dickens, G. R., C. K. Paull, P. J. Wallace, and ODP Leg 164 Scientific Party, 1997, Direct measurement of *in situ* methane quantities in a large gas-hydrate reservoir: *Nature*, v. 385, p. 426-428.
- Dugan, B., and P. B. Flemings, 2000, Overpressure and Fluid Flow in the New Jersey Continental Slope: Implications for Slope Failure and Cold Seeps: *Science*, v. 289, p. 288-291.
- Egorov, A. V., K. Crane, P. R. Vogt, and A. N. Rozhkov, 1999, Gas hydrates that outcrop on the sea floor: Stability models: *Geo-Marine Letters*, v. 19, p. 68-75.
- Etiopie, G., and R. W. Klusman, 2002, Geologic emissions of methane to the atmosphere, *in* J. M. Adams, ed., *Chemosphere (Oxford)*, v. 49, p. 777-789.
- Flemings, P. B., B. B. Stump, T. Finkbeiner, and M. Zoback, 2002, Flow focusing in overpressured sandstones: theory, observations, and applications: *American Journal of Science*, v. 302, p. 827-855.
- Gaarenstroom, L., R. A. J. Tromp, M. C. de Jong, and A. M. Brandenburg, 1993, Overpressures in the Central North Sea: implications for trap integrity and drilling safety: *Petroleum Geology of Northwest Europe: 4th Conference*, p. 1305-1313.
- Ham, H. H., 1966, A method of estimating formation pressures from Gulf Coast well logs: *Transactions - Gulf Coast Association of Geological Societies*, v. 16, p. 185-197.
- Harrison, W. J., and L. L. Summa, 1991, Paleohydrology of the Gulf of Mexico Basin: *American Journal of Science*, v. 291, p. 109-176.
- Hart, B. S., P. B. Flemings, and A. Deshpande, 1995, Porosity and pressure; role of compaction disequilibrium in the development of geopressures in a Gulf Coast Pleistocene basin: *Geology*, v. 23, p. 45-48.
- Hubbert, M. K., and D. G. Willis, 1972, Mechanics of Hydraulic Fracturing: *Memoir - American Association of Petroleum Geologists*, v. 18, p. 239-257.
- Kohl, B., and H. H. Roberts, 1994, Fossil foraminifera from four active mud volcanoes in the Gulf of Mexico: *Geo-Marine Letters*, v. 14, p. 126-134.
- Lerche, I., and E. Bagirov, 1998, Guide to gas hydrate stability in various geological settings: *Marine and Petroleum Geology*, v. 15, p. 427-437.
- Lupa, J., P. B. Flemings, and S. Tennant, 2002, Pressure and trap integrity in the deepwater Gulf of Mexico: *The Leading Edge*, v. 21, p. 184 - 187.
- Milkov, A. V., 2000, Worldwide distribution of submarine mud volcanoes and associated gas hydrate: *Marine Geology*, v. 167, p. 29-42.
- Milkov, A. V., and R. Sassen, 2001, Estimate of gas hydrate resource, northwestern Gulf of Mexico continental slope: *Marine Geology*, v. 179, p. 71-83.

- Neurauter, T. W., and W. R. Bryant, 1990, Seismic expression of sedimentary volcanism on the continental slope, northern Gulf of Mexico: *Geo-Marine Letters*, v. 10, p. 225-231.
- Rafalowski, J. W., B. W. Regel, D. L. Jordan, and D. O. Lucidi, 1994, Green Canyon Block 205 lithofacies, seismic facies, and reservoir architecture, *in* P. Weimer, and T. L. Davis, eds., *AAPG Studies in Geology* 42, v. 42: Tulsa, OK, AAPG/SEG, p. 133-142.
- Ritger, S., B. Carson, and E. Suess, 1987, Methane-derived authigenic carbonates formed by subduction-induced pore-water expulsion along the Oregon/Washington margin; with Suppl. Data 87-02: *Geological Society of America Bulletin*, v. 98, p. 147-156.
- Roberts, H. H., and P. Aharon, 1994, Hydrocarbon-derived carbonate buildups of the northern Gulf of Mexico continental slope; a review of submersible investigations: *Geo-Marine Letters*, v. 14, p. 135-148.
- Roberts, H. H., and R. S. Carney, 1997, Evidence of Episodic Fluid, Gas and Sediment Venting on the Northern Gulf of Mexico Continental slope: *Economic Geology*, v. 92, p. 863-879.
- Roberts, H. H., R. Sassen, and A. V. Milkov, 2001, Seafloor Expression of Fluid and Gas Expulsion from Deep Petroleum Systems, Continental Slope of the Northern Gulf of Mexico: *GCSSEPM Foundation Annual Research Conference*, p. 407-421.
- Rowan, M. G., 1995, Structural Styles and Evolution of Allochthonous Salt, Central Louisiana Outer Shelf and Upper Slope, *in* M. P. A. Jackson, D. G. Roberts, and S. Snelson, eds., *Salt tectonics: A global perspective: AAPG Memoir*, 65, p. 119-225.
- Rowan, M. G., and P. Weimer, 1998, Salt-sediment interaction, north Green Canyon and Ewing Bank (offshore Louisiana) northern Gulf of Mexico: *AAPG Bulletin*, v. 82, p. 1055-1082.
- Rubey, W. W., and M. K. Hubbert, 1959, Overthrust belt in geosynclinal area of western Wyoming in light of fluid-pressure hypothesis, 2: Role of fluid pressure in mechanics of overthrust faulting: *GSA Bulletin*, v. 70, p. 167-205.
- Sassen, R., A. V. Milkov, E. Ozgul, H. H. Roberts, J. L. Hunt, M. A. Beeunas, J. P. Chanton, D. A. DeFreitas, and S. T. Sweet, 2003, Gas venting and subsurface charge in the Green Canyon area, Gulf of Mexico continental slope: evidence of a deep bacterial methane source?: *Organic Geochemistry*, v. 34, p. 1455-1464.
- Sassen, R., S. T. Sweet, A. V. Milkov, D. A. DeFreitas, and M. C. Kennicutt, II, 2001, Thermogenic vent gas and gas hydrate in the Gulf of Mexico slope; is gas hydrate decomposition significant?: *Geology*, v. 29, p. 107-110.
- Somoza, L., V. Díaz-del-Río, R. León, M. Ivanov, M. C. Fernández-Puga, J. M. Gardner, F. J. Hernández-Molina, L. M. Pinheiro, J. Rodero, A. Lobato, A. Maestro, J. T. Vázquez, T. Medialdea, and L. M. Fernández-Salas, 2003, Seabed Morphology and hydrocarbon seepage in the Gulf of Cádiz mud volcano area: Acoustic imagery, multibeam and ultra-high resolution seismic data: *Marine Geology*, v. 195, p. 153-176.
- Swarbrick, R. E., M. J. Osborne, D. Grunberger, G. S. Yardley, G. Macleod, A. C. Aplin, S. R. Larter, I. Knight, and H. A. Auld, 2000, Integrated study of the Judy Field (Block 30/7a) - an overpressured Central North Sea oil/gas field: *Marine and Petroleum Geology*, v. 17, p. 993-1010.
- Turcotte, D. L., and G. Schubert, 2002, *Geodynamics*: Cambridge, Cambridge University Press.
- Yardley, G. S., and R. E. Swarbrick, 2000, Lateral transfer; a source of additional overpressure?: *Marine and Petroleum Geology*, v. 17, p. 523-537.
- Yin, P., Z. Liu, S. Berné, P. Vagner, and B. Loubrieu, 2003, Mud volcanoes at the shelf margin of the East China Sea: *Marine Geology*, v. 194, p. 135-149.
- Yuvancic-Strickland, B., E. J. Kuhl, T. W. Lee, B. J. Seldon, P. B. Flemings, and T. Ertekin, 2003, Integration of Geologic Model and Reservoir Simulation, Popeye Field, Green Canyon 116: 53rd Annual Gulf Coast Association of Geological Societies.

# INTEGRATION OF GEOLOGIC MODEL AND RESERVOIR SIMULATION, POPEYE FIELD, GREEN CANYON 116

Beth Yuvancic-Strickland<sup>1</sup>, Eric Kuhl<sup>2</sup>, Tin-Wai Lee<sup>1</sup>, Benjamin Seldon<sup>1</sup>, Peter B. Flemings<sup>1</sup>, and Turgay Ertekin<sup>2</sup>

<sup>1</sup>Pennsylvania State University, Department of Geosciences, University Park, PA 16802; E-mail: flemings@geosc.psu.edu

<sup>2</sup>Pennsylvania State University, Department of Petroleum and Natural Gas Engineering, University Park, PA 16802; E-mail: turgay@pnge.psu.edu

## ABSTRACT

Small variations in fault length, channel permeability, and aquifer volume defined in our geologic model of the G-sand strongly influence flow characteristics, and hence the predicted recovery from the RA reservoir in the Popeye field (Gulf of Mexico, GC 72/116). A history-matched base-case reservoir simulation, with structure and rock properties derived from the geologic model, results in a volume of bypassed gas-condensate in the RA reservoir. Turbidite gravity flows entered the basin from the north and deposited amalgamated sheet sands. This was overlain by channels that bypassed the Popeye area, depositing interbedded very fine-grained sands and silts in levee-overbank environments. A channel and impermeable faults compartmentalize the G-sand into four gas-condensate reservoirs (RA, RB, RM and RN). By increasing the distance between two faults separating the RA and RB reservoirs, decreasing the RA aquifer volume, or increasing channel permeability in the reservoir model, flow characteristics in the RA reservoir change. These changes, which reflect the geologic uncertainties in our interpretation, result in economically significant differences in total recovery.

## INTRODUCTION

Numerous reservoirs are found in turbidite deposits within minibasins on the continental slope of the northern Gulf of Mexico deep-water (Fig. 1). In this tabular-salt minibasin province, intraslope minibasins develop from salt withdrawal due to sediment loading (Diegel et al., 1995). The resultant bathymetry focuses gravity flows into these areas of localized accommodation (Rowan and Weimer, 1998). This depositional process accumulated the high quality sands described at Bullwinkle (Holman and Robertson, 1994), Genesis (Rafalowski et al., 1994), Mensa (Pfeiffer et al., 2000), Mars (Mahaffie, 1994), and Auger fields (Booth et al., 2000; McGee et al., 1994).

Characterizations of the Weyburn (Elsayed et al., 1993) and Ram-Powell (Lerch et al., 1996) fields and a depositional model for the Bullwinkle field (Holman and Robertson, 1994) were created

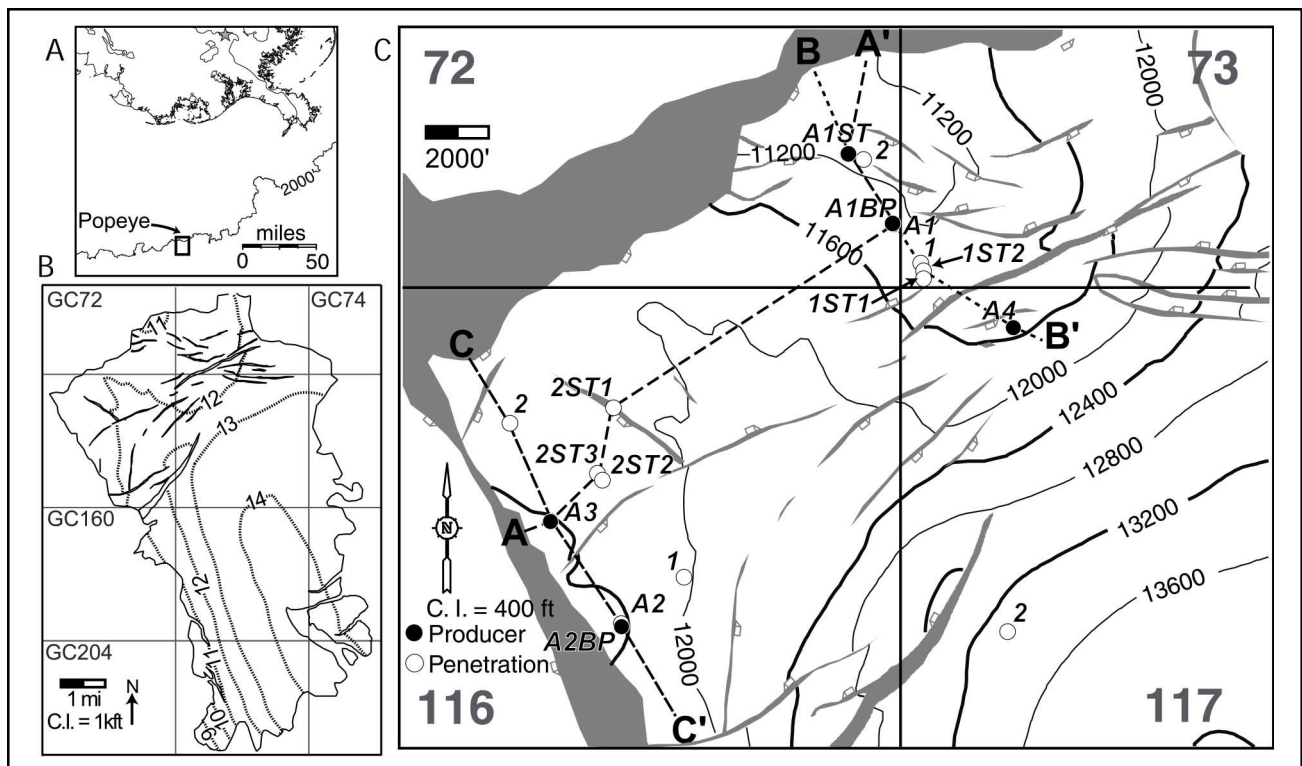


Figure 1: A) The Popeye field is located 140 miles southwest of New Orleans in 2000 ft of water. B) Structure map of vertical subsea depth (TVDSS) to the top of the G-sand in the minibasin. This map was created by mapping the trough minima of the G-sand reflector and depth-converting it using known penetration depths at well locations. C) Expanded view of structure map, focused on the Popeye field. Line A-A' is displayed on Figure 3; A-A', B-B', and C-C' are displayed on Figure 7.

by integrating seismic, well, core and production data. These analyses served as a foundation for reservoir simulations. At Mensa, integration of engineering data into reservoir simulations further refined the geologic model (e.g. Pfeiffer et al., 2000).

This study incorporates geological, geophysical and engineering data to characterize the G-sand reservoir at Popeye. The reservoir is complicated by lithologic variation, fault compartmentalization and an erosional channel. Reservoir simulations are used to refine our geologic model and identify a volume of bypassed reserves. Modification of uncertain geologic properties affects the producibility of these reserves.

## GEOLOGIC OVERVIEW

### Regional Setting

Popeye is a subsea development located in Green Canyon Blocks 72, 73, 116 and 117 (Fig. 1). It is in the northern, proximal, part of a larger minibasin (Figs. 1B, 1C) that includes the Genesis field (GC 205/161) on the western flank of the minibasin (Varnai, 1998; Rafalowski et al., 1994). Gas and condensate are produced from the late Pliocene (Fig. 2) G-sand reservoir, at 11,500 ft (3505 m) depth (Fig. 1). Production from the four G-sand reservoir compartments (RN and RM in the west, RA and RB in the northeast) (Fig. 3) is tied back to the Cougar platform in South Timbalier Block 300, 24 miles (38.6 km) to the north.

The Popeye field is situated between a salt-stock system to the west and an extensional salt tongue to the east (Weimer et al., 1998). The field is on the southern downthrown side of a regional growth fault (Fig. 3). The RM and RN reservoirs are bounded on the west by a normal fault that dips to the southwest. Smaller faults and a channel compartmentalize the G-sand into four reser-

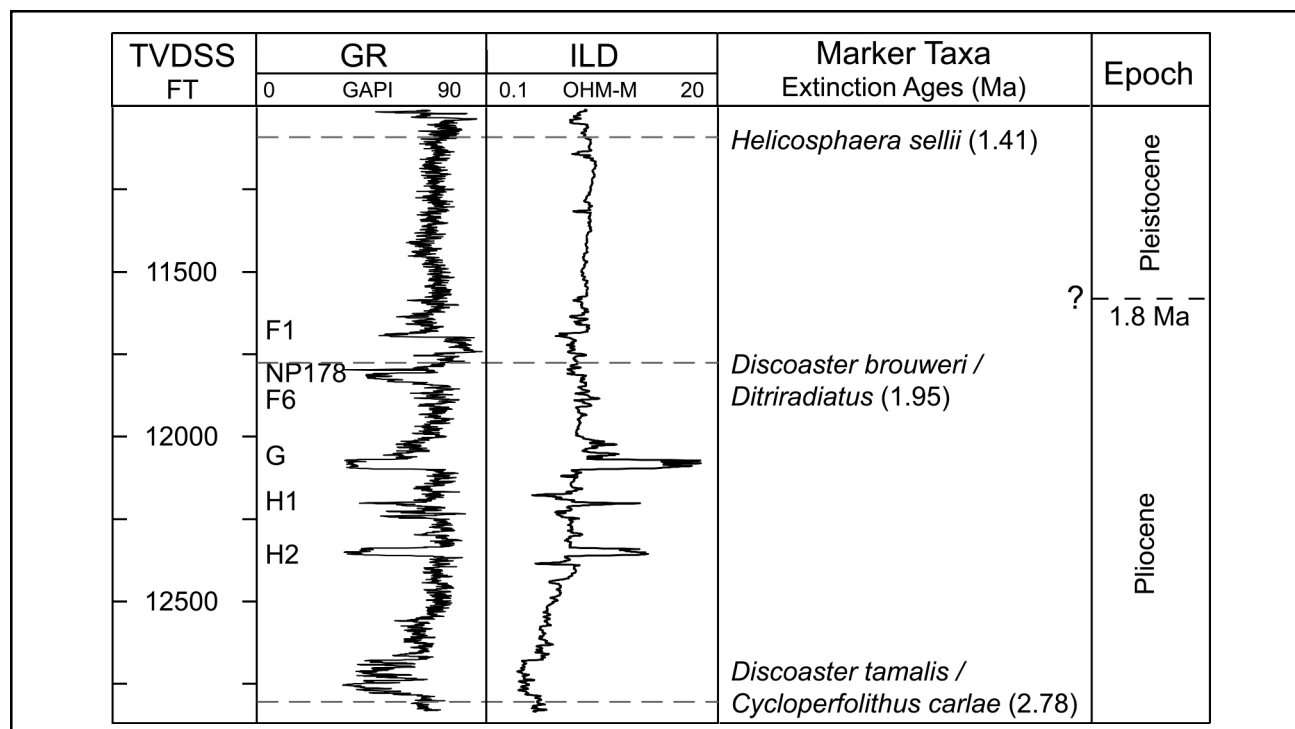


Figure 2: Gamma-ray (GR) and resistivity (ILD) logs for the 116-1 well (located in Figure 1). Biostratigraphic markers and correlated extinction ages (Styzen, 1996) are shown. The projection of the Pliocene-Pleistocene boundary is estimated.

voirs (Fig. 3). Large negative amplitudes delineate gas accumulations in the structural highs of these compartments; the gas-water contacts (GWCs) are generally parallel to depth-structure contours (Figs. 3, 4).

### The G-Sand

Well-log data reveal that the G-sand reservoir consists of laminated facies ( $G_L$ ) and an underlying massive facies ( $G_M$ ) that averages 75 ft (22.9 m) in gross thickness (Fig. 5). The  $G_L$  is a very fine-grained, high porosity sandstone that is interbedded with silty shale (Fig. 5; Table 1). The  $G_M$  is a fine-grained, clean sandstone with no internal structure and moderate sorting (Table 1). It has a clean, blocky log signature with a sharp base (Fig. 5).

Table 1.  $G_L$  and  $G_M$  Rock Properties

Facies	Bedding	Net-to-Gross (%)	Sand Grain Size	Sand Porosity (%)	Sw (%)
GL	cm scale beds	11 - 79	very fine	25 - 30	13 - 40
GM	massive	88 - 100	fine	30 - 35	6 - 15

The  $G_L$  is mostly shale in the RN reservoir and has the most sand in the RA reservoir (Fig. 5). The  $G_L$  in the RM compartment becomes sandier with depth, indicated by a ramped log signature (Fig. 5B). Across much of the RA compartment, the  $G_L$  is capped by a clean, 10-ft sand (Fig. 5, red arrow). Beneath this sand, the  $G_L$  also has a ramped signature (Fig. 5C). Velocity and density are highest where the  $G_L$  is shaliest (RN) (Fig. 5A) and lowest where the  $G_L$  is sandiest (RA) (Fig. 5C). As a result, the  $G_L$  has the highest acoustic impedance in the RN reservoir, is intermediate in the RM reservoir, and is lowest in the RA reservoir.

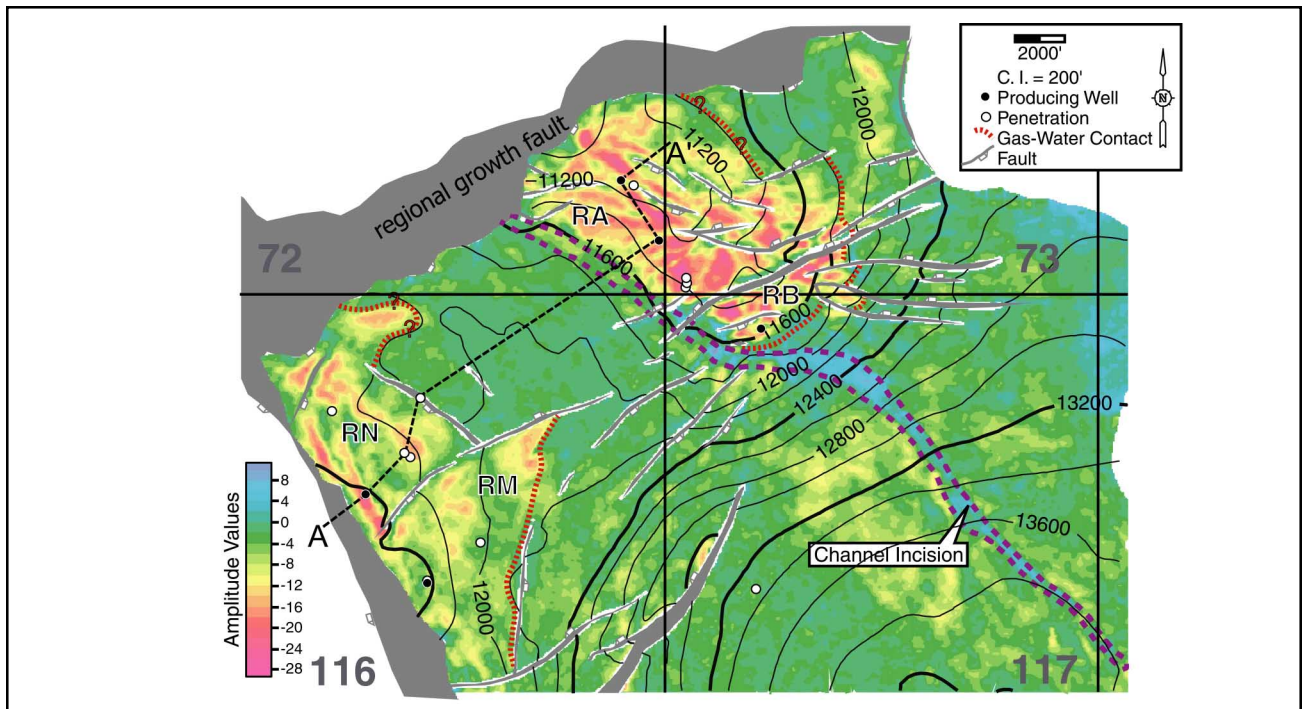


Figure 3: The amplitude of the G-sand trough with contours of the depth (TVDSS) to the top of the  $G_1$ .

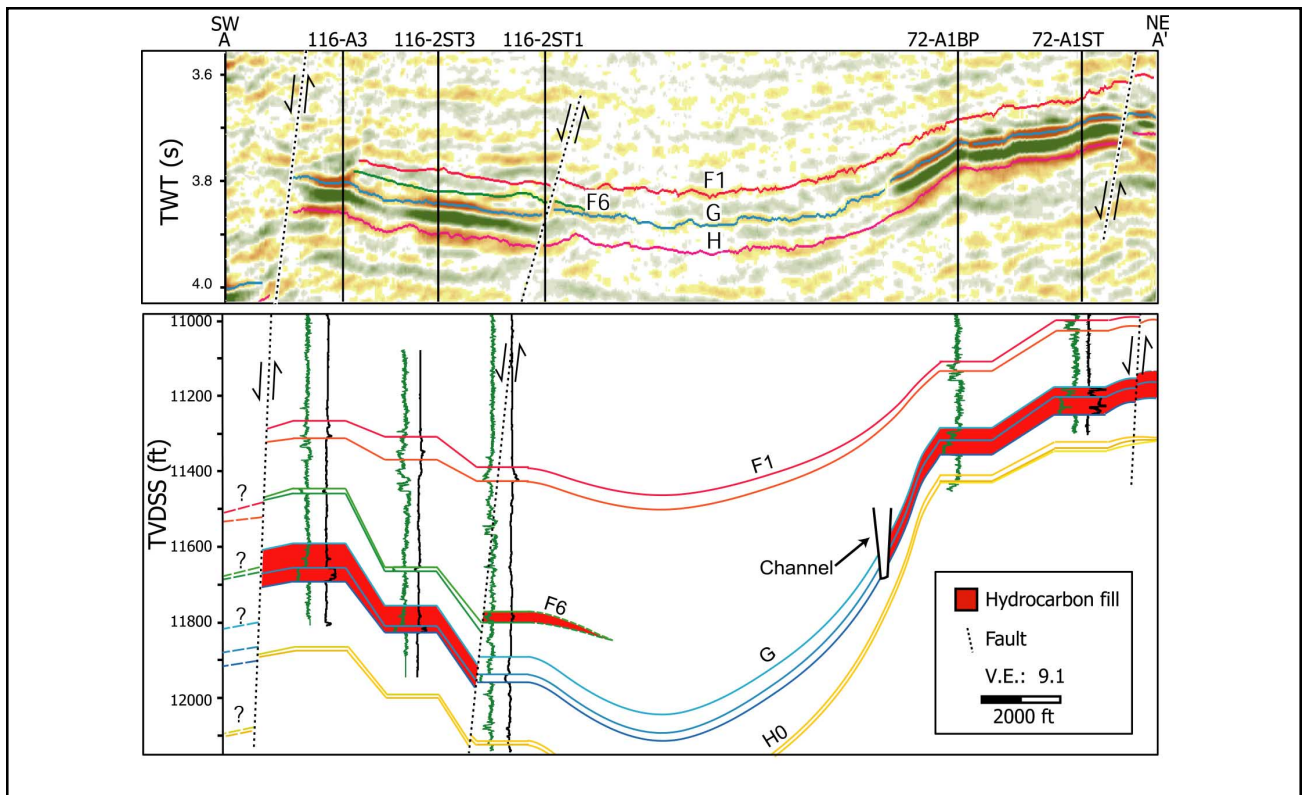


Figure 4: A) Seismic cross-section A-A' (located in Figure 1). Reds are negative values (troughs) and blues are positive values (peaks). The aquifer area between the RN and RA reservoirs exhibits a chaotic, discontinuous, low amplitude response. The H0, H1, and H2 sands cannot be distinguished in seismic data and are mapped as the H-group sands. B) Structural cross-section along A-A'. The erosional channel is the western limit of gas accumulation in the RA/RB reservoirs.

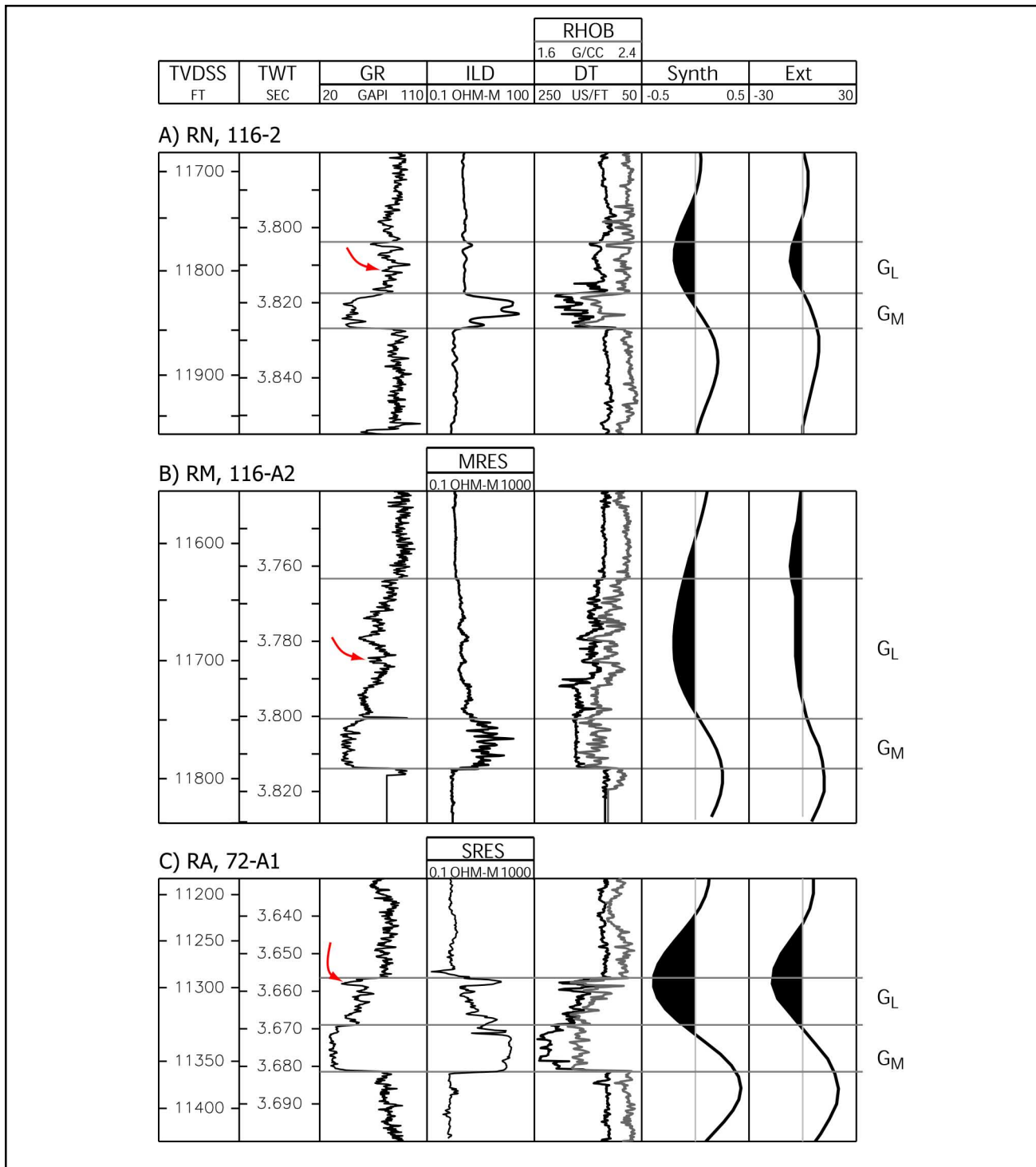


Figure 5: Seismic and log response (located in Figure 1C) in each compartment. The synthetic (Synth) and extracted (Ext) seismograms are zero-phase and were created with a 12-Hz Ricker wavelet. The extracted seismograms were shifted up 46 ms at well 116-2, 116 ms up at well 116-A2, and 58 ms up at well 72-A1 relative to the synthetic seismograms, due to poor velocity control. The correlatable sand body discussed in text is identified by red arrows on GR log. A) The  $G_L$  is not imaged in the RN reservoir. B) In the RM compartment, the trough is broad and asymmetric. C) The entire G-sand is imaged with a strong trough at the top and a strong peak at the base.

The relationship between seismic loop and sand geometry varies across the field. In the RN reservoir there is little impedance contrast between the  $G_L$  and the overlying shales, and a strong contrast between the  $G_L$  and  $G_M$  (Fig. 5A). As a result, the  $G_L$  is not seismically imaged and the  $G_M$  drives the seismic response. The  $G_M$  is also below tuning thickness (~80 ft or 24 m), so the seismic trough is above the top of the  $G_M$  and the seismic peak is below the  $G_M$  base. In the RM compartment, the thick  $G_L$  that shales upwards produces synthetic seismograms that show a broad, asymmetric trough whose minima is below the top of the  $G_L$  and a narrow peak that aligns with the base of the  $G_M$  (Fig. 5B). Although the RM reservoir has more sand in the  $G_L$  than the RN reservoir, amplitudes of the RN and RM reservoirs are comparable. The RA reservoir has the greatest impedance contrast between the  $G_L$  and the overlying shales due to the capping sand, and the smallest impedance contrast between the  $G_L$  and  $G_M$  (Fig. 5C). Seismograms in the RA show symmetric troughs that align with the top of the  $G_L$  and peaks that align with the base of the  $G_M$ . The RA compartment has the most negative amplitudes in the field.

No simple correlation between seismic attributes (e.g. amplitude and loop thickness) and log properties (gross thickness, net thickness, and net-to-gross ratio) of the G-sand or its individual facies was found. The only general trend is that the thick, clean sands of the RA compartment have brighter amplitudes. As a result, there was no consistent way to use seismic attributes to map the thickness or quality of the G-sand away from the well penetrations.

Repeat formation tests (RFTs), taken prior to production, were used to characterize Popeye reservoir pressures (Fig. 6). Gas-phase pressures were extrapolated vertically from their well locations along a gas gradient (0.13 psi/ft, 5.7 MPa/m) to each components GWC and reservoir crest. Pressures within the aquifer were assumed to follow a hydrostatic gradient (0.465 psi/ft, 20.5 MPa/m) with the water pressure equal to the gas pressure at the GWC. The RA and RN water pressures are similar. In contrast, the RM aquifer pressures are approximately 150 psi (1.03 MPa) lower (Fig. 6). The pre-production RM pressures do not follow a gas gradient and we debate the quality of these data.

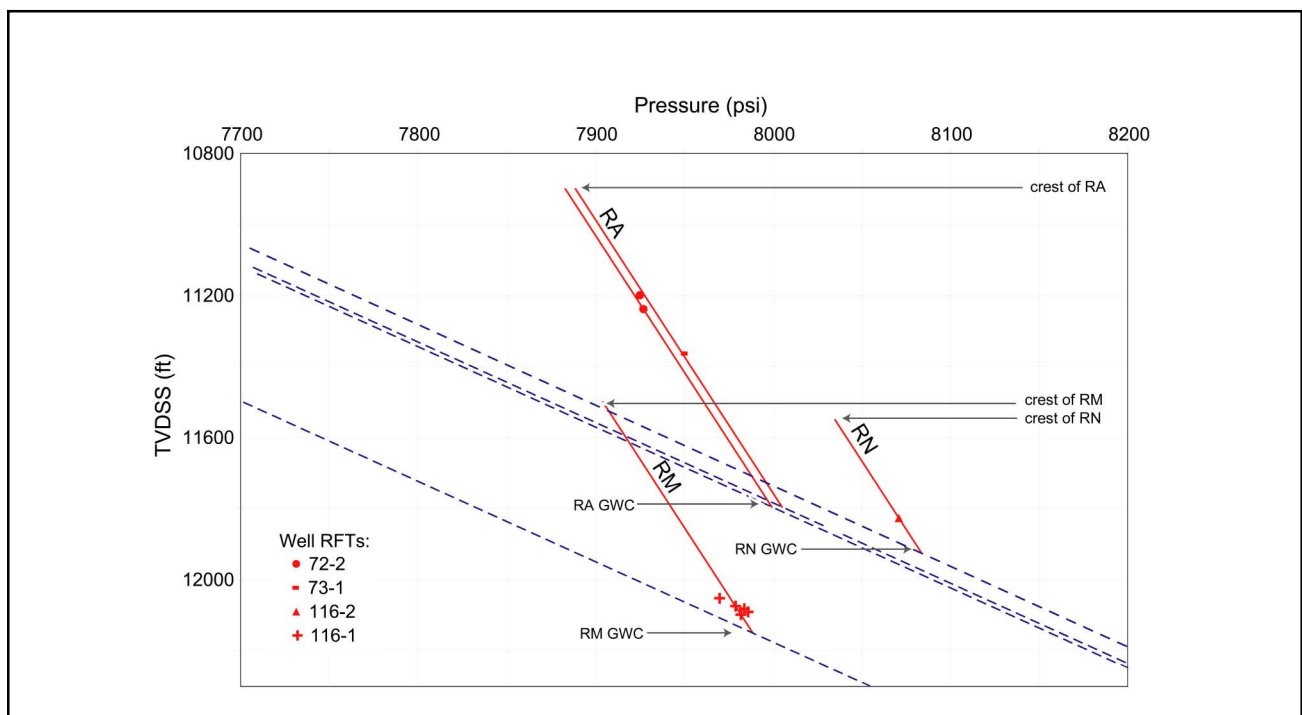


Figure 6: Initial pressures in the G-sand at Popeye. Gas pressures (red) and inferred aquifer pressures (blue solid lines) intersect at mapped GWCs. The RA and RN have similar aquifer pressures whereas the RM reservoir has a lower aquifer pressure.

## GEOLOGIC OBSERVATIONS AND DEPOSITIONAL MODEL

The RA and RB reservoirs contain the thickest  $G_M$  deposits; the  $G_L$  is thickest in the southwest area of the field (Figs. 7, 8). The  $G_M$  is thickest along a northwest-southeast trend through the RA and RB reservoirs (Figs. 7A, 7B). The  $G_L$  thins from the southwest to the northeast decreasing away from the RM reservoir (Figs. 7C, 7D, 8A, 8C). In the RA reservoir, the  $G_M$  has the lowest gamma-ray values, velocity, density, and the brightest amplitudes (Fig. 5C), which indicate the  $G_M$  is cleaner here than elsewhere in the field.

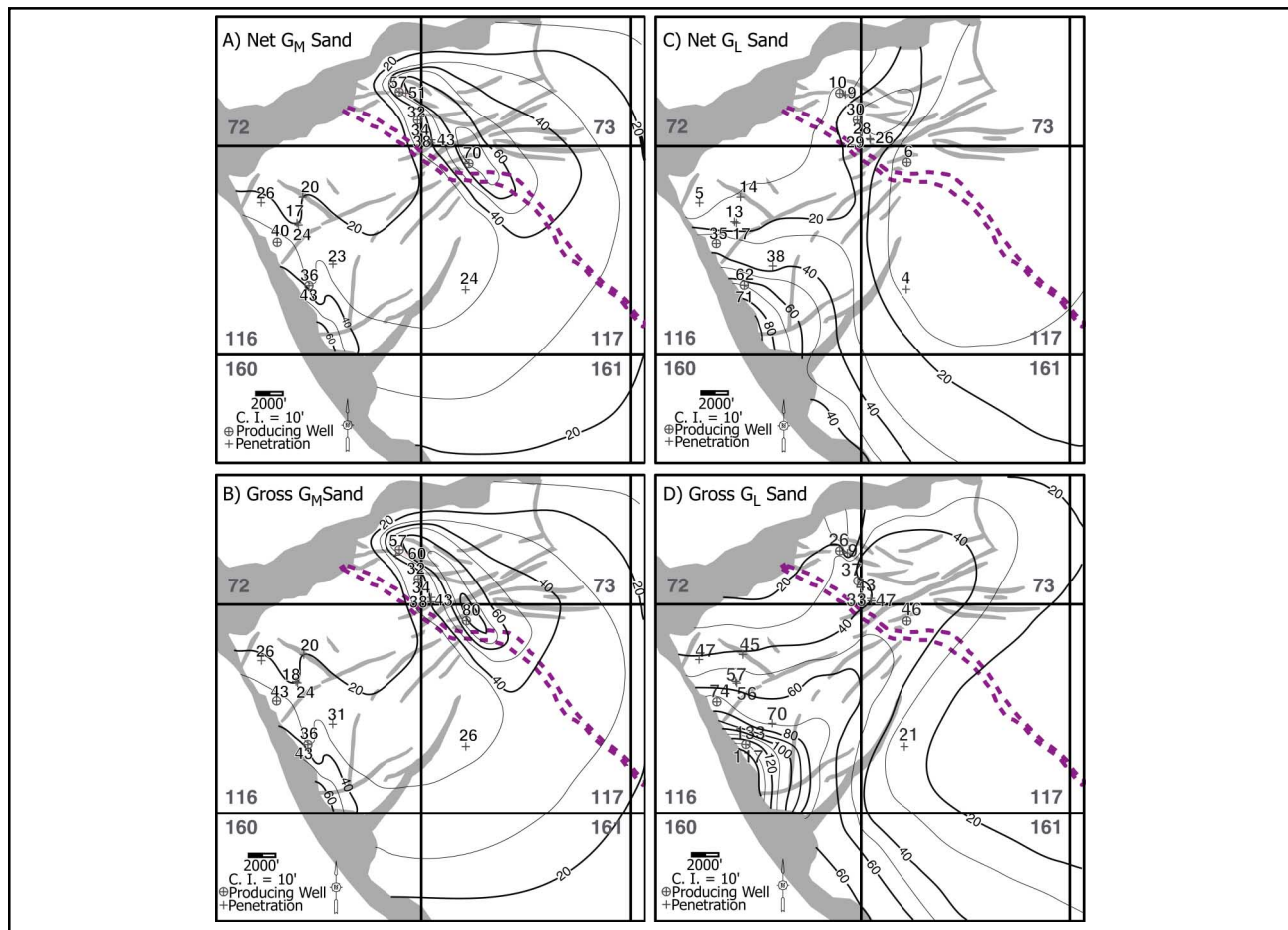


Figure 7: Net and gross G-sand thicknesses based on well data, seismic reflection character and depositional model. A and B) Net and gross  $G_M$  distributions are similar due to the high  $G_M$  net-to-gross ratio. C and D) Thickest net and gross  $G_L$  are located in the RM reservoir.

A sand body is correlated across the RA, RN, and RM reservoirs within the  $G_L$  facies (Figs. 5, 8). This sand is observed at the top of the  $G_L$  within the RA reservoir, and is thinner and located in the middle of the  $G_L$  in the RM and RN reservoirs (Figs. 5, 8). The  $G_L$  below this sand body has constant thickness from northeast to southwest across the field (Fig. 8A).

Due to the variability of seismic attributes in relation to  $G_L$  and  $G_M$  thickness and sand quality, sand distribution maps were largely based on well penetration information, a depositional model, and general trends in the seismic response. The lithologic and pore fluid variations of the G-sand and resulting seismic response are reflected in map view (Fig. 3). Aquifer regions contain small amplitudes with coherent reflections south of the RB and RM compartments. However, the aquifer region between the RA and RN reservoirs has a chaotic, discontinuous seismic reflection (Fig. 4). The G-sand seismic loop thins, amplitudes decrease, and the reflection becomes less continuous down to the south and east in the minibasin.

Positive amplitudes (Fig. 3) show a small channel of different lithology running through the center of the field. This indicates the channel was filled by sediments post-dating the G-sand with higher acoustic impedance properties. A seismic reflection isochron map between the G-sand and the underlying H-Sands reveals the geometry of a channel within the G-sand entering the basin south of the RM reservoir, oriented northwest southeast (Fig. 9).

### ***Interpretation***

The difference in sand thickness trends between the  $G_M$  and  $G_L$  are interpreted to record two different depositional mechanisms. Gravity flows at G-sand time entered the basin north of well A1ST and deposited thick sheet sands (Figs. 10, 11). We infer low-relief bathymetry within the slope accommodation space slowed gravity flows, depositing sand while finer-grained sediments continued downslope. The localized linear pattern of the thickest  $G_M$  occurrences (Figs. 7A, 7B) indicates that the  $G_M$  was deposited in a bathymetric low, produced either by erosion from prior flows or the flows themselves. Abrupt changes in local gradients, such as the northern growth fault (Fig. 3), have been shown to cause incision and flow confinement (Friedmann et al., 2000).

After the local accommodation space was filled with the  $G_M$  sediment entry into the minibasin changed. The  $G_L$  was deposited by levee-overbank sedimentation from the channel south of the RM reservoir and by channels traveling through the central part of the field (Figs. 7, 11). The chaotic nature of the G-sand reflection indicates that post-depositional erosion of the  $G_M$  by channels bypassing this area disrupted sand continuity (Figs. 10, 11). The vertical position of the correlatable sand within the  $G_L$  (Fig. 8) indicates that overbank sedimentation from the channel south of the RM reservoir provided the last significant  $G_L$  deposits in the Popeye area (Figs. 8, 11).

Features interpreted at Popeye are consistent with nearby fields and regional trends. The Genesis field, seven miles south of Popeye, contains sinuous, elongate channels that trend northwest to southeast in reservoir sands (Rafalowski et al., 1994), indicating a consistent sediment transport direction through this area. Winker and Booth (2000) describe how in a proximal, typically bypass facies assemblage area of a minibasin, ponded sediment such as the  $G_M$  can accumulate. A small change in relief south of the Popeye reservoir area induced sand to drop from gravity flows, depositing the  $G_M$  (Fig. 10). Once slope equilibrium was reached, levee deposits covered the area forming the  $G_L$ .

Prather et al. (1998) suggests that a lithologic transition analogous to the  $G_M$ -to- $G_L$  change records the natural fill progression of accommodation in a slope minibasin. Alternatively, a eustatic interpretation suggests that rapid sea level fall forced erosion of the shelf, sourcing the turbidite sheet sands on the continental slope. This is followed in late lowstand by deposition of finer sediments in channel-levee complexes (Posamentier et al., 1991; Carminatti and Scarton, 1991).

## **PRODUCTION HISTORY**

Production from Popeye began in January 1996 from wells A1BP and A2BP. As of June 2003, the field produced 329 billion cubic feet (BCF) of gas from 5 wells. The A3 well went online in January 1998, has produced 68 BCF, and currently produces 20 million standard cubic feet per day (MMSCF/D) (6/25/03). The A1BP well was shut-in due to completion problems in January 1999 after producing 47 BCF. It was replaced by well A1ST which produces 59 MMSCF/D (6/25/03) and has produced 75 BCF (6/25/03). In April 2002, the A2BP well was shut-in due to water production; it produced 125 BCF. At this time the A4 well came online, now producing 29 MMSCF/D (6/25/03) with cumulative production of 17 BCF (6/25/03).

## **RESERVOIR SIMULATION**

### ***Base-Case Model Description***

A three-dimensional, compositional reservoir simulator is used to match production and pressure data. The  $G_L$  and  $G_M$  are represented by separate layers; each layer has its distinct and constant

rock properties (Table 2), relative permeability curves, and is divided into 10,000 grid blocks. Layer thicknesses are derived from Figure 7, structural geometry from Figure 3, and relative permeabilities from a database constrained by absolute permeability and fluid type. Core experiments provide capillary curves, used to determine initial water saturations (Fig. 13B) and a compaction model (Ostermeier, 1993; Ostermeier, 2001).

**Table 2. Constant Property Values Assigned to Simulation Layers in Reservoir Model.**

Layer	Porosity (%)	$k_h$ (mD)	$k_v$ (mD)	$Sw_{irr}$	$Sg_r$	Initial Compressibility (1/psi)
$G_L$	25	500	0.1	0.143	0.021	$22.21 \cdot 10^{-6}$
$G_M$	30	1200	500	0.119	0.022	$22.21 \cdot 10^{-6}$

The four hydrocarbon compartments are assumed to be in pressure communication through a common down-dip aquifer (Fig. 6). The G-sand is represented by six equalization regions composed of four reservoir compartments and two aquifer regions, each with different initial compositions, PVT properties, and GWCs (Fig. 13A). Grid boundaries and faults are assumed to be impermeable (Figs. 13A, 13B).

An Equation of State (EOS) model is created for each reservoir compartment based on fluid samples taken from producing wells. These EOS models are simplified into a set of six pseudo-components whose properties are varied to match the behavior of the original fluid samples in PVT experiments, using a process similar to that of Coats (1985).

The history match for the field is based on bottom-hole pressures, daily production rates, and cumulative production. History matching was an iterative process of modifying the geologic model, the GWCs, and aquifer support. The historical data are matched for the field, with the gas rates specified (Fig. 12).

The reservoir model is used to predict future well performance. The most intriguing result of the base-case simulation is that a pocket of gas will not be produced south of the A1ST well in the RA reservoir (Fig. 13C). The A1ST well is offset 900 ft (274 m) southwest and 80 ft (24 m) deeper than the crest of the RA anticline. A cluster of faults is oriented parallel to the anticline; these faults slow fluid flow through the area which causes the development of two primary flow paths (Fig. 13A). Pathway A develops just up-dip from the RA-RB bounding fault and Pathway B is north of the fault cluster. In this initial simulation, Pathway B dominates and well A1ST waters out before the gas, structurally beneath the well, is produced (Fig. 13C).

### ***Modifications of the Base-Case Model***

Simulations were performed to understand how 1) flow path constriction into the RA reservoir, 2) aquifer thickness, and 3) channel permeability, affect the drainage behavior. Each of these properties was varied and history matches were obtained, allowing for comparisons of unproduced reserves in the RA reservoir. Pathway A runs between the two faults that separate the RB and RA reservoirs (Fig. 13A, purple arrow). If the separation of these two faults is increased, then aquifer support to the RA reservoir is increased and flow along Pathway A dominates (Fig. 13A). As a result, more of the gas pocket is produced by the present well than in the base case scenario (Table 3). If the thickness of the northeast portion of the RA reservoir, represented by a dim amplitude area, (Figs. 3, 13) is decreased by 50%, the flow along Pathway B is reduced and more of the gas pocket can be produced by the present wells (Table 3). Finally, if the channel west of the RA reservoir is only partially sealing (transmissibility multiplier of 0.01) there is added water drive from the west. This eliminates the pocket of bypassed reserves south of the A1ST; reserves remain north of the A1ST well (Table 3).

Table 3. Difference in RA Reservoir Production for Simulations with Uncertain Reservoir Properties.

Simulation	Initial Gas Volume in RA Reservoir (MMSCF)	Production from RA Reservoir	Difference (MMSCF)
Base Case	304,867	219,989	84,887
Fault Separation Increase	304,867	224,963	79,913
Decrease in RA Aquifer Thickness	285,698	227,773	57,925
Channel Transmissibility Increase (*0.001)	304,867	218,959	85,917

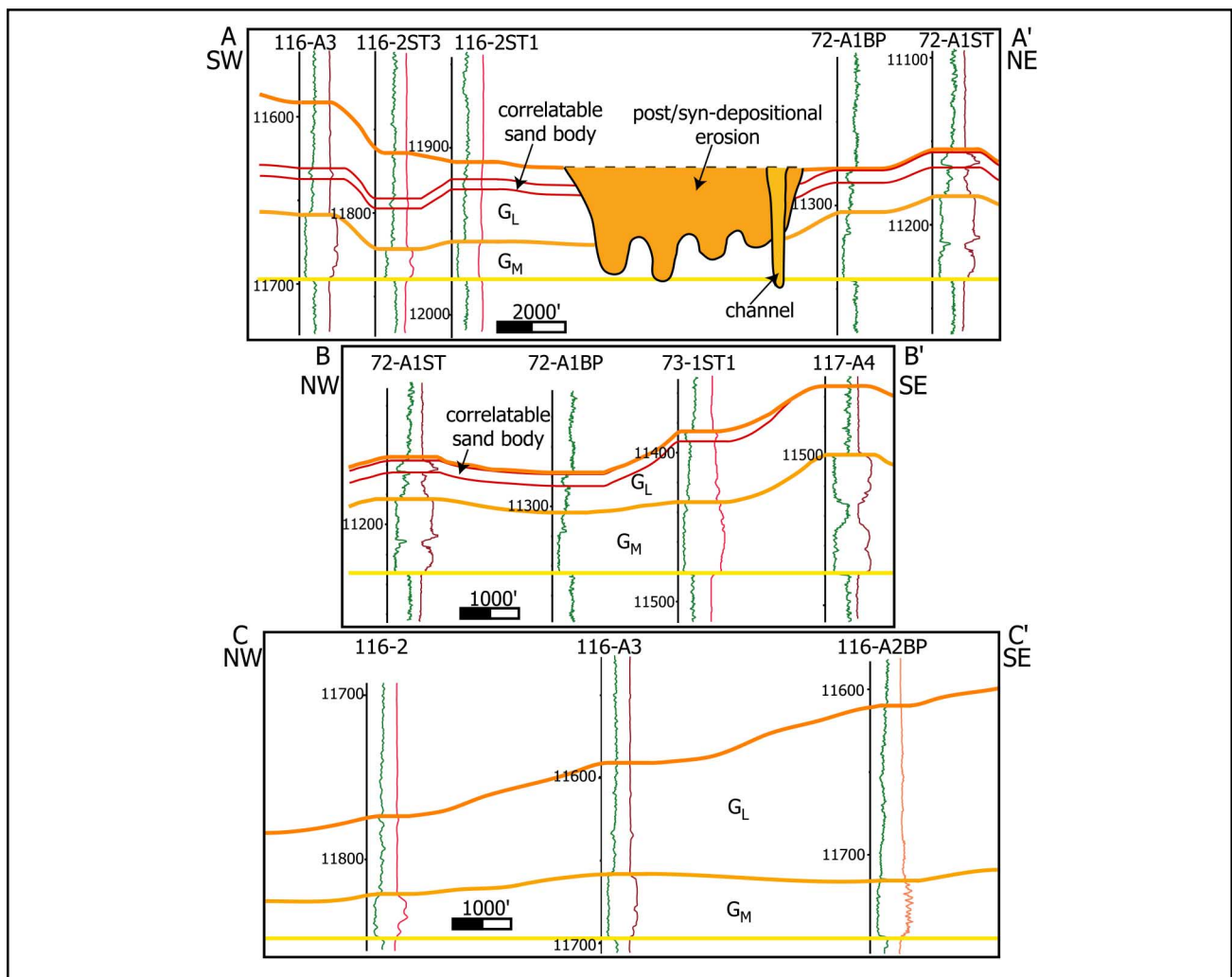


Figure 8: Stratigraphic cross-sections flattened to the G-sand base. A) G<sub>L</sub> thickens to the southwest, closer to the channel that sourced levee deposits. B) Although well 72-A1ST is closest to sediment-entry point, the thickest G<sub>M</sub> accumulations occur in RB, possibly due to preexisting bathymetry. C) G<sub>L</sub> deposits thicken towards the channel that enters basin south of RM reservoir. Sections are located in Figure 1.

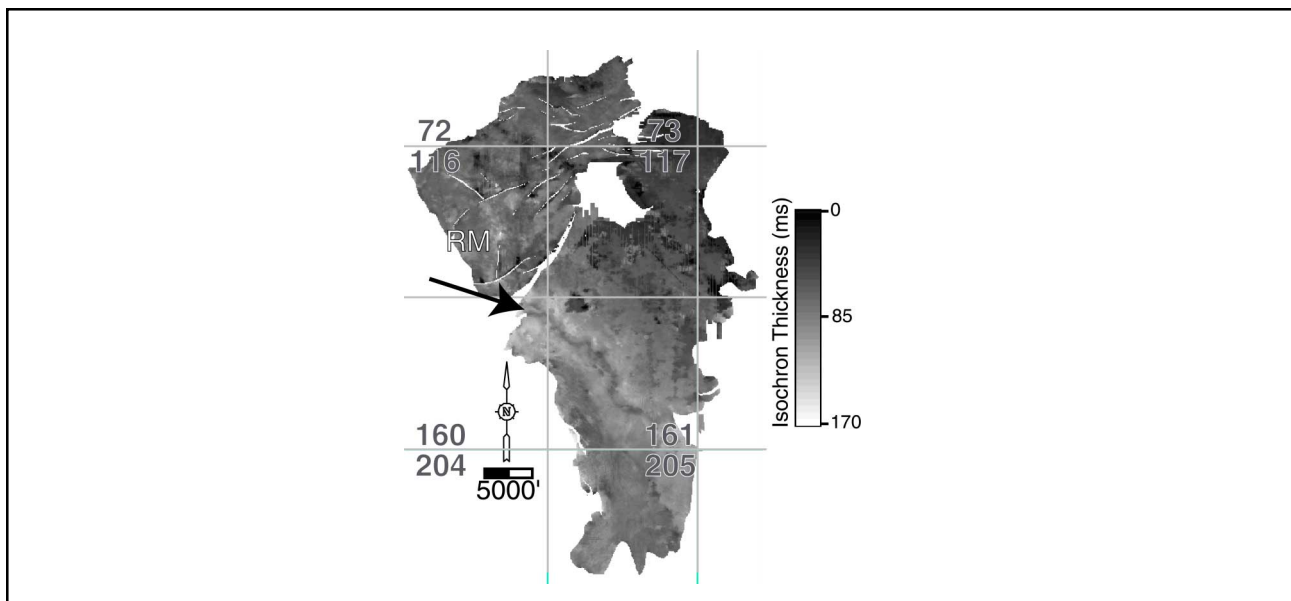


Figure 9: Isochron map in two-way time (ms) between the G-sand and underlying H-sands. A channel bypassing the Popeye area at G-sand time enters the basin south of the RM reservoir, providing significant  $G_L$  sediments to the RM reservoir.

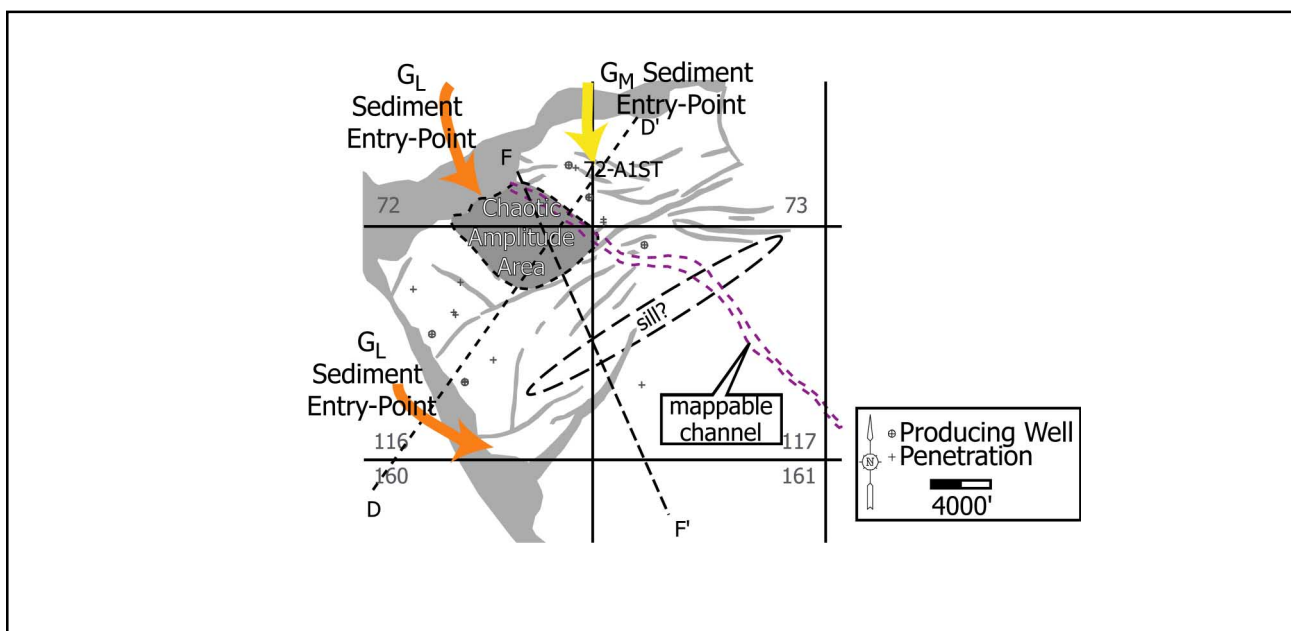


Figure 10: Interpreted features of the G-sand. The colored arrows identify sediment-entry points in our depositional model.

These simulations illustrate that uncertainty in the geologic model propagates to uncertainty in reservoir performance. Simulations show that future pressure measurements from well A1ST should distinguish between the four simulation scenarios, however, the down-hole and tubing head pressure gauges have failed and a special effort would be required to obtain these data. In addition, a more detailed analysis of fault throw might be used to better constrain zones of fault impermeability. Unfortunately, there are no well penetrations in the aquifer east of the RA to better constrain the thickness. Finally, while it is geologically reasonable that the channel is impermeable, further investigation using time-lapse seismic or well test analysis might verify fluid displacement and determine the permeability of the channel.

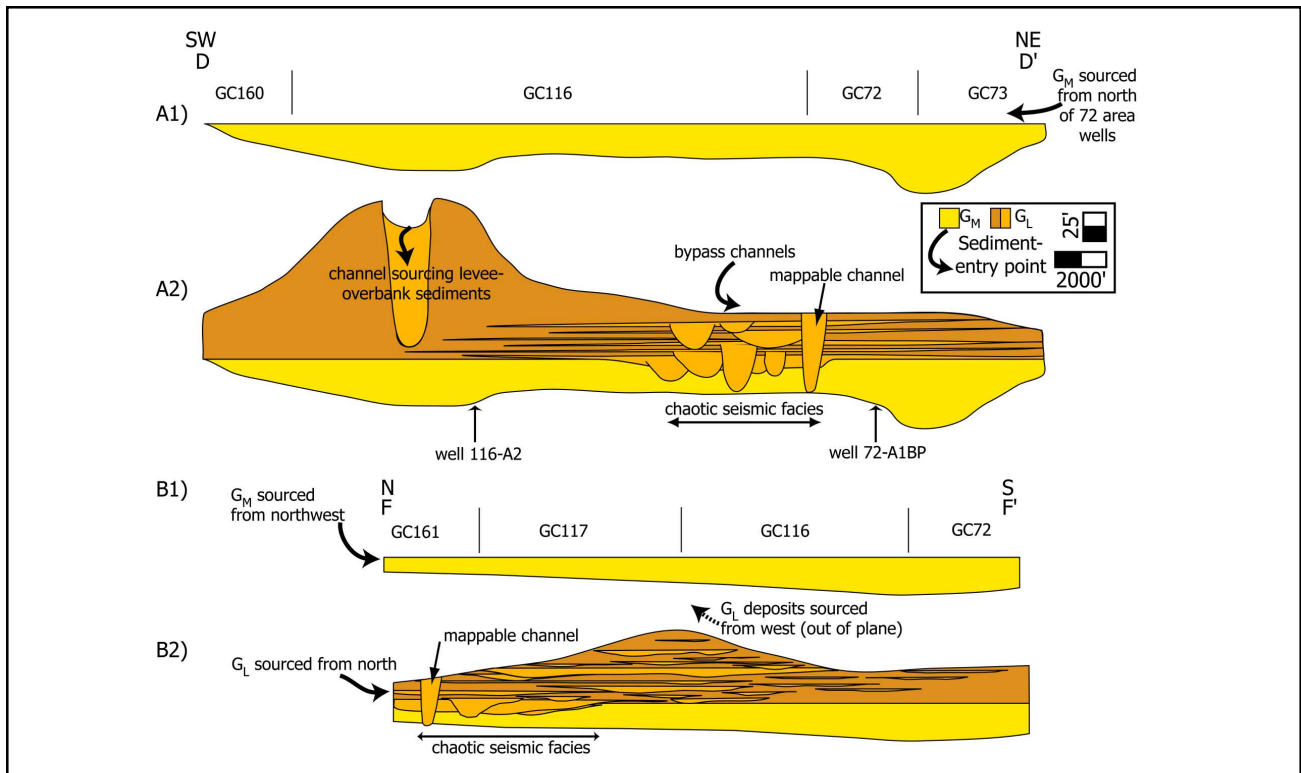


Figure 11: Model of G-sand deposition, in strike view (A, B) and dip view (C, D). A, C) Sediment enters basin as sheet flows from an area north of well 72-A1ST (Fig. 10). Successive flows into the basin amalgamate, forming the  $G_M$ . B, D) The sediment-entry point switches to the central portion of the field and channels bypass the Popeye area. Levee deposits accumulate across the field, thickest in the southwest. Bypassing channels incise deposits and create a chaotic seismic signature. Sediment input ends and the G-sand is capped by mud. The locations of cartoon cross-sections are in Figure 10.

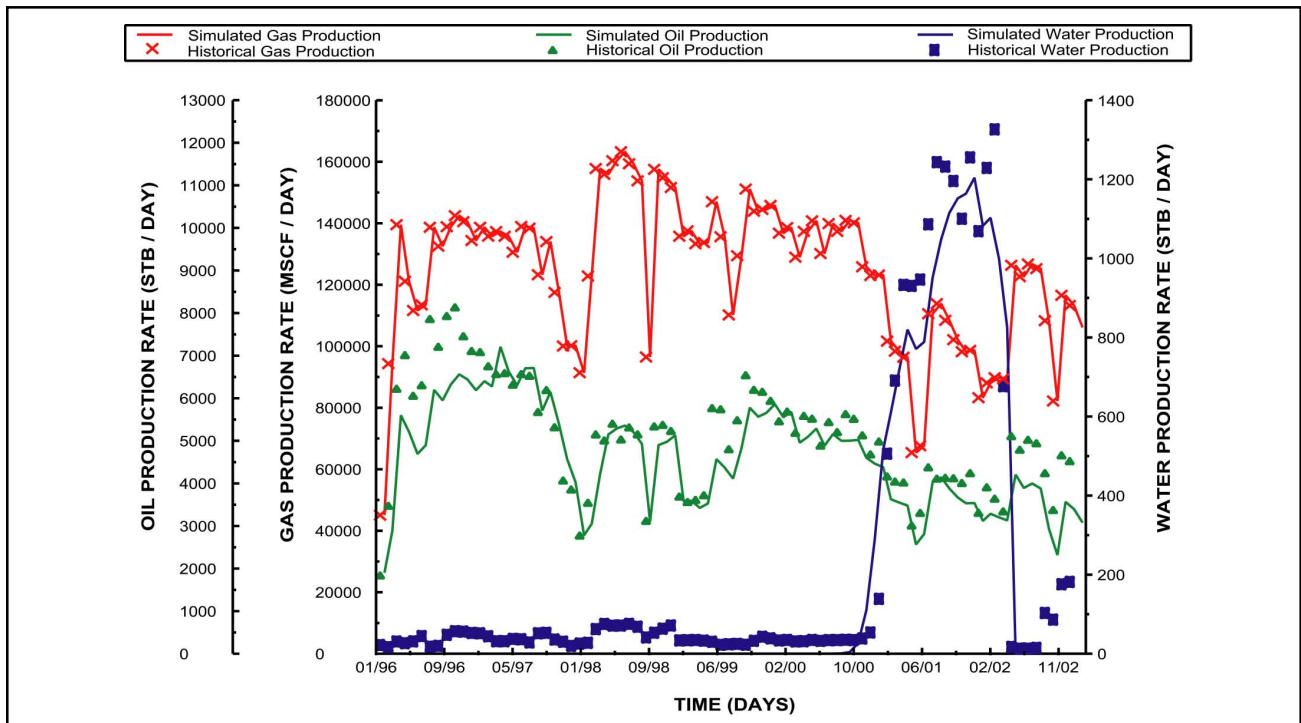


Figure 12: History match for the Popeye field from January 1996 to December 2002.

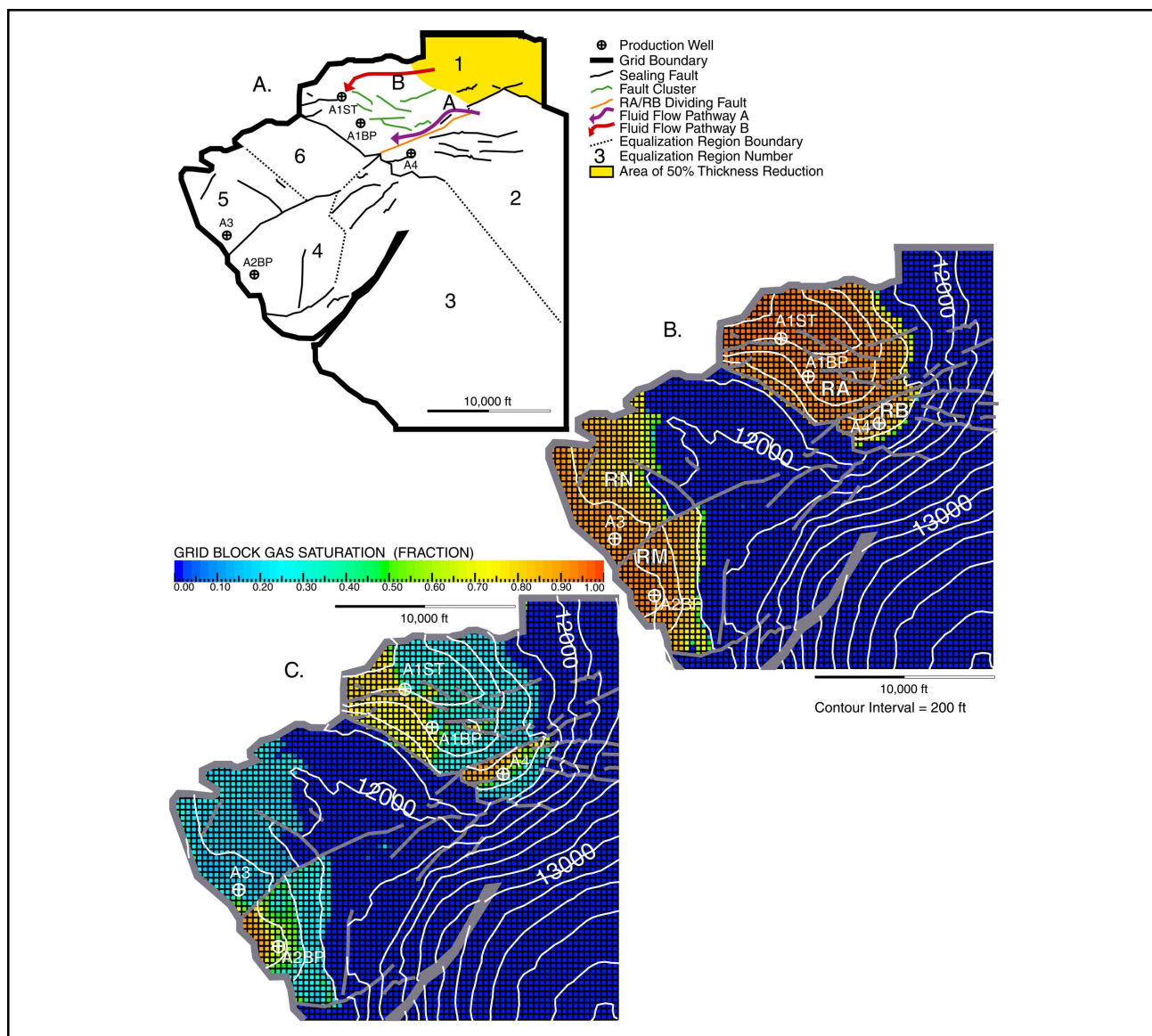


Figure 13: A) Equalization regions and boundary conditions for the Popeye reservoir simulator. The hydrocarbon bear regions are 1, 2, 4, and 5; 3 and 6 are aquifer regions. B) Initial gas saturation in the  $G_M$  layer (01/01/1996). Initially there is 761 BCF gas in place. C) Final gas saturation of the  $G_M$  layer using the current producing wells (09/01/2001). Notice the pocket of non-produced hydrocarbons to the west and south of the A1BP well.

## CONCLUSIONS

Well log, engineering, and seismic data were integrated to develop a depositional model. The massive facies ( $G_M$ ) was deposited by gravity flows that entered the basin north of the RA reservoir. These amalgamated sheet sands were overlain by laminated sands ( $G_L$ ) and silts deposited by levee-overbank sedimentation from bypass channels. This depositional model provides constraints for the sand distribution interpretations used in reservoir simulations.

The base-case reservoir simulation results in a volume of bypassed reserves within the RA reservoir. The simulated location and amount of unrecovered reserves can differ based on the modeled fault separation between the RA and RB reservoirs, RA aquifer volume, and channel transmissibility. Expanding the distance between the two faults separating the RA and RB reservoirs or decreasing the RA aquifer volume increases the volume of bypassed reserves, while in-

creasing the channel permeability changes the location of unrecovered reserves. These reasonable variations in the geologic model significantly influence reservoir drainage behavior.

## ACKNOWLEDGMENTS

We thank Rob Sloan, Dick Eikmans, Dave Miller, Scott Baker, Anne Burke, and others in the SEPCo Green Canyon Development Team. The Shell Foundation, SEPCo, Chevron-Texaco, Amerada Hess, Anadarko, Landmark Graphics, and Penn State University all support the Geosystems Initiative, of which this work is a part.

## REFERENCES

- Booth, J., DuVernay III, A., Pfeiffer, D., and Styzen, M., 2000. Sequence stratigraphic framework, depositional models, and stacking patterns of ponded and slope fan systems in the Auger basin: central Gulf of Mexico slope: GCSSEPM Foundation 20<sup>th</sup> Annual Research Conference, Deep-water Reservoirs of the World, p. 82-103.
- Carminatti, M. and Scarton, J. C., 1991. Sequence stratigraphy of the Oligocene turbidite complex of the Campos Basin, offshore Brazil: An overview, in Weimer, P. and Link, M. H., eds., *Seismic Facies and Sedimentary Processes of Submarine Fans and Turbidite Systems*: New York, Springer-Verlag, p. 241-246.
- Coats, K. H., 1985. Simulation of gas condensate reservoir performance: *Journal of Petroleum Technology*, vol. 37, no. 11, p. 1870-1885.
- Diegel, F.A., Karlo, J. F., Schuster, D. C., Shoup, R. C., and Tauvers, P. R., 1995. Cenezoic structural evolution and tectonostratigraphic framework of the northern Gulf Coast continental margin, in Jackson, M. P. A., Roberts, D. G., and Snelson, S., eds., *Salt Tectonics: A Global Perspective*: Tulsa, OK, AAPG, p. 109-151.
- Elsayed, S. A., Baker, R., Churcher, P. I., and Edmunds, A. C., 1993. Multidisciplinary characterization and simulation study of the Weyburn Unit: *Journal of Petroleum Technology*, vol. 45, no. 10, p. 930-934, 973.
- Friedmann, S. J., Beaubouef, R. T., Pirmez, C., and Jennette, D. C., 2000. The effects of gradient changes on deep-water depositional systems: an integrated approach: AAPG 2000 annual meeting, vol. 2000, p. 51.
- Holman, W. E. and Robertson, S. S., 1994. Field development, depositional model, and production performance of the turbidic "J" sands at Prospect Bullwinkle, Green Canyon 65 fields, outer-shelf Gulf of Mexico, in Weimer, P., Bouma, A. H., and Perkins, B. F., eds., *Submarine Fans and Turbidite Systems—Sequence Stratigraphy, Reservoir Architecture, and Production Characteristics*: GCSSEPM, 15<sup>th</sup> Annual Research Conference, p. 139-150.
- Lerch, C. S., Bramlett, K. W., Butler, W. H., Scales, J. N., Stud, T. B., and Glandt, CA., 1996. Integrated 3D reservoir modeling at Ram-Powell field: A turbidite reservoir in the eastern Gulf of Mexico: Proceedings—SPE Annual Technical Conference and Exhibition, *Sigma*, p. 477-492.
- Mahaffie, M. J., 1994. Reservoir classification for turbidite intervals to the Mars discovery, Mississippi Canyon 807, Gulf of Mexico, in Weimer, P., Bouma, A. H., and Perkins, B. F., eds., *Submarine Fans and Turbidite Systems—Sequence Stratigraphy, Reservoir Architecture, and Production Characteristics*: GCSSEPM, 15<sup>th</sup> Annual Research Conference, p. 233-244.
- McGee, D. T., Bilinski, P. W., Gary, P. S., Pfeiffer, D. S., and Sheiman, J. L., 1994. Geologic models and geometries of Auger field, deep-water Gulf of Mexico, in Weimer, P., Bouma, A. H., and Perkins, B. F., eds., *Submarine Fans and Turbidite Systems—Sequence Stratigraphy, Reservoir Architecture, and Production Characteristics*: GCSSEPM, 15<sup>th</sup> Annual Research Conference, p. 245-256.
- Ostermeier, R.M., 1993. Deep-water Gulf of Mexico turbidites: compaction effects on porosity and permeability: *SPE Formation Evaluation*, vol. 10, no. 2, p. 79-85.
- Ostermeier, R.M., 2001. Compaction effects on porosity and permeability: Deep-water Gulf of Mexico turbidites: *Journal of Petroleum Technology*, vol. 53, no. 2, p. 68-74.
- Pfeiffer, D., Mitchell, B., and Yevi, G., 2000. Mensa, Mississippi Canyon block 731 field, Gulf of Mexico—an integrated field study: GCSSEPM Foundation 20<sup>th</sup> Annual Research Conference, Deep-water Reservoirs of the World, p. 756-775.
- Posamentier, H. W., Erskine, R. D., and Mitchum Jr., R. M., 1991. Models for submarine-fan deposition with in a sequence stratigraphic framework, in Weimer, P. and Link, M. H., eds., *Seismic Facies and Sedimentary Processes of Submarine Fans and Turbidite Systems*: New York, Springer-Verlag, p. 127-136.
- Prather, B. E., Booth, J. R., Steffens, G. S., and Craig, P.A., 1998. Classification, lithologic calibration and stratigraphic succession of seismic facies of intraslope basins, deep-water Gulf of Mexico: *AAPG Bulletin*, v.82, no. 5A, p. 701-728.

- Rowan, M. and Weimer, P., 1998. Salt-sedimentation interaction, northern Green Canyon and Ewing Bank (offshore Louisiana), northern Gulf of Mexico: AAPG Bulletin, v. 82, no. 5B, p. 1055-1082.
- Rafalowski, J. W., Regel, B. W., Jordan, D. L., and Lucidi, D. O., 1994. Green Canyon Block 205 lithofacies, seismic facies, and reservoir architecture, in P. Weimer and T. L. Davis, eds., AAPG Studies in Geology 42, Tulsa, OK, AAPG/SEG, p. 133-142.
- Styzen, M., 1996. Late Cenozoic chronostratigraphy of the Gulf of Mexico: GCSSEPM Foundation, Houston, TX.
- Varnai, P., 1998. Three-dimensional seismic stratigraphic expression of Pliocene-Pleistocene turbidite systems, northern Green Canyon (offshore Louisiana), Northern Gulf of Mexico: AAPG Bulletin, v. 82, no. 5B, p. 986-1012.
- Weimer, P., Rowan, M. G., McBride, B. C., and Kligfield, R., 1998. Evaluating the petroleum systems of the northern deep Gulf of Mexico through integrated basin analysis: an overview: AAPG Bulletin, v. 82, no. 5B, p. 865-877.
- Winker, C. and Booth, J., 2000. Sedimentary dynamics of salt-dominated continental slope, Gulf of Mexico: integration of observations from the seafloor, near-surface, and deep subsurface: GCSSEPM Foundation 20<sup>th</sup> Annual Research Conference, Deep-water Reservoirs of the World, p. 1059-1086.